REPORT DOCUMENTATION PAGE	Form Approved OMB NO. 0704-0188

1. AGENCY USE ONLY (Leave Blank)	2. REPORT DATE:	3. REPORT TYPE AND DATES COVERED
	1-Jun-2007	Final Report 1-Jun-2003 - 30-Nov-2006

4. TITLE AND SUBTITLE

Theoretical Analysis of Control Mechanisms for Boundary-Layer Separation on Rotorcraft Blades

5. FUNDING NUMBERS

DAAD19-03-1-0127

6. AUTHORS

Philip A. Blythe

8. PERFORMING ORGANIZATION REPORT NUMBER

7. PERFORMING ORGANIZATION NAMES AND ADDRESSES

Lehigh University
526 Brodhead Avenue, 23

Bethlehem, PA 18015 -3046

9. SPONSORING/MONITORING AGENCY NAME(S) AND ADDRESS(ES)

U.S. Army Research Office
P.O. Box 12211
Research Triangle Park, NC 27709-2211

10. SPONSORING / MONITORING AGENCY REPORT NUMBER

45029-EG.1

11. SUPPLEMENTARY NOTES

The views, opinions and/or findings contained in this report are those of the author(s) and should not contrued as an official Department of the Army position, policy or decision, unless so designated by other documentation.

12. DISTRIBUTION AVAILIBILITY STATEMENT

Approved for public release; distribution unlimited

12b. DISTRIBUTION CODE

13. ABSTRACT (Maximum 200 words)

The abstract is below since many authors do not follow the 200 word limit

14. SUBJECT TERMS

Unsteady three dimensional separation, oscillating blades, leading edge suction.

15. NUMBER OF PAGES

Unknown due to possible attachments

16. PRICE CODE

17. SECURITY CLASSIFICATION OF REPORT	18. SECURITY CLASSIFICATION ON THIS PAGE	19. SECURITY CLASSIFICATION OF ABSTRACT	20. LIMITATION OF ABSTRACT
UNCLASSIFIED	UNCLASSIFIED	UNCLASSIFIED	UL

Report Title

Theoretical Analysis of Control Mechanisms for Boundary-Layer Separation on Rotorcraft Blades

ABSTRACT

High maneuverability is one of the major goals in rotorcraft design. In practice, this goal is limited by unsteady (dynamic) stall near blade leading edges. Studies of three-dimensional boundary layer separation on a rotating blade are made. For hovering flight, the blade twist and downwash are included in the effective angle of attack. For forward flight, high angles of attack are used to simulate the most severe situation at the retreating blade. Because of the disparate scales of the leading edge radius and the blade span, separation is found to be quasi two-dimensional, and local singular behaviors at separation are very similar to the two-dimensional cases. Most of the results are obtained using an Eulerian approach, but a Lagrangian formulation is used to study the behavior near the separation singularity. Control mechanisms based on suction and blade oscillations are examined. It is found that oscillations, with a tuned frequency and amplitude, can delay separation. Leading edge suction/injection is also effective in delaying separation for particular (optimized) slot locations.

List of papers submitted or published that acknowledge ARO support during this reporting period. List the papers, including journal references, in the following categories:

(a) Papers published in peer-reviewed journals (N/A for none)

Number of Papers published in peer-reviewed journals: 0.00

(b) Papers published in non-peer-reviewed journals or in conference proceedings (N/A for none)

Number of Papers published in non peer-reviewed journals: 0.00

(c) Presentations

Number of Presentations: 0.00

Non Peer-Reviewed Conference Proceeding publications (other than abstracts):

Number of Non Peer-Reviewed Conference Proceeding publications (other than abstracts): 0

Peer-Reviewed Conference Proceeding publications (other than abstracts):

Number of Peer-Reviewed Conference Proceeding publications (other than abstracts): 0

(d) Manuscripts

Number of Manuscripts: 0.00

Number of Inventions:

Graduate Students

NAME	PERCENT_SUPPORTED
Xiaofeng Zou	1.00
Lixiang Luo	0.02
FTE Equivalent:	**1.02**
Total Number:	**2**

Names of Post Doctorates

NAME	PERCENT_SUPPORTED
FTE Equivalent:	
Total Number:	

Names of Faculty Supported

NAME	PERCENT_SUPPORTED	National Academy Member
Philip A. Blythe	0.09	No
FTE Equivalent:	**0.09**	
Total Number:	**1**	

Names of Under Graduate students supported

NAME	PERCENT_SUPPORTED
FTE Equivalent:	
Total Number:	

Student Metrics

This section only applies to graduating undergraduates supported by this agreement in this reporting period

The number of undergraduates funded by this agreement who graduated during this period:	0.00
The number of undergraduates funded by this agreement who graduated during this period with a degree in science, mathematics, engineering, or technology fields:.....	0.00
The number of undergraduates funded by your agreement who graduated during this period and will continue to pursue a graduate or Ph.D. degree in science, mathematics, engineering, or technology fields:.....	0.00
Number of graduating undergraduates who achieved a 3.5 GPA to 4.0 (4.0 max scale):	0.00
Number of graduating undergraduates funded by a DoD funded Center of Excellence grant for Education, Research and Engineering:	0.00
The number of undergraduates funded by your agreement who graduated during this period and intend to work for the Department of Defense	0.00
The number of undergraduates funded by your agreement who graduated during this period and will receive scholarships or fellowships for further studies in science, mathematics, engineering or technology fields:	0.00

Names of Personnel receiving masters degrees

NAME
Total Number:

Names of personnel receiving PHDs

NAME
Total Number:

Names of other research staff

NAME	PERCENT_SUPPORTED
FTE Equivalent:	
Total Number:	

Sub Contractors (DD882)

Inventions (DD882)

THEORECTIAL ANALYSIS OF CONTROL MECHANISMS FOR BOUNDARY LAYER SEPARATION ON ROTORCRAFT BLADES

by

X. Zou and P. A. Blythe

Department of Mechanical Engineering & Mechancis

Lehigh University

Contents

List of Figures

Abstract

High maneuverability is one of the major goals in rotorcraft design. In practice, this goal is limited by unsteady (dynamic) stall near blade leading edges. Studies of three-dimensional boundary layer separation on a rotating blade are made. For hovering flight, the blade twist and downwash are included in the effective angle of attack. For forward flight, high angles of attack are used to simulate the most severe situation at the retreating blade. Because of the disparate scales of the leading edge radius and the blade span, separation is found to be quasi two-dimensional, and local singular behaviors at separation are very similar to the two-dimensional case. Most of the results are obtained using an Eulerian approach, but a Lagrangian formulation is used to study the behavior near the separation singularity. Control mechanisms based on suction and blade oscillations are examined. It is found that oscillations, with a tuned frequency and amplitude, can delay separation. Leading edge suction/injection is also effective in delaying separation for particular (optimized) slot locations.

Chapter 1

Introduction

1.1 Background

Dynamic stall refers to a series of events on pitching airfoils during unsteady flight. Stall is usually initiated by boundary layer separation near the leading edge, and culminates in the formation of a dynamic stall vortex accompanied by a strong interaction between the viscous inner flow and the inviscid outer flow. This can result in a severe loss of lift and an abrupt increase in pitching moment. During changing flight conditions, dynamic stall plays a decisive role in restricting airfoil performance. In experiments, it is usually observed that a primary vortex forms and resides on the upper surface of an airfoil, accompanied by a considerable increase in the lift. This extra gain in lift, however, is not sustained. A secondary or even tertiary vortex is quickly seen beneath the primary one and the interaction between these vortices ultimately causes the primary vortex to leave the surface and travel downstream. As a result, the flow field is strongly disturbed and the airfoil performance is severely limited.

Dynamic stall is the major impediment to enhancing the performance of rotating blades. Currently, two approaches are used to control dynamic stall. One approach is involved with keeping the stall vortex on the airfoil surface so that the beneficial aspect of dynamic stall can be retained. Marginal separation theory may shed some light in this direction, but adequate theories or effective experimental methods are not yet available. The second approach is concerned with techniques for suppressing or inhibiting separation at high angles of attack. These techniques are based on delaying the vorticity eruption that gives rise to stall.

Unsteady separation control cannot be achieved in a conventional way. A primary difficulty is that the boundary layer near the leading edge evolves over a local time scale that is much smaller than a global time scale associated with the chord length (airfoil pitching, wake shedding etc., are all related to the chord length). A global time scale $[T]$ can be defined as the interval in which a blade advances a half

chord. As an specific example, if the chord length $c = 0.5ft$ and the free stream velocity $U_o = 350ft/s$, then the global time size is $[T] = \frac{c}{2U_o}] = \frac{1}{1400}s$. A local time can be estimated by $[t] = \frac{r_o}{U_o}$, where $r_o = R_o\epsilon^2(c/2)$, is the radius of the leading edge. ϵ is the thickness length ratio of an airfoil and R_o is a constant. For NACA0012 airfoil, $\epsilon = 0.12$ and $R_o = 1.1$. Simple arithmetic shows that the absolute value of $[t]$ is very small, say around 10^{-5} second; it is less than $1/70$ of the global scale. Therefore, any event inside the boundary layer is difficult to capture in experiments, especially in a helicopter environment involving a variety of complex fluid phenomena.

Another reason for the failure of a conventional strategy lies in the fact that boundary layer separation initiates in very small spatial scales above the airfoil surface. Even at the instant prior to separation, measurable features on the wall such as surface pressure or wall shear do not signal the onset of separation. Thus methods for separation prevention can not be actuated by a precursor detection. In order to be effective, control should interfere at an early time.

A closer look at the physics of unsteady separation may be helpful before implementing any control mechanism. The development of unsteady separation near the leading edge of an airfoil can be characterized by two stages. In the first stage, the adverse pressure gradient on the upper surface causes gradual deceleration of the flow inside the boundary layer and strong vorticity diffusion at the wall. In two-dimensional flow the vorticity $\omega \approx \dfrac{\partial u}{\partial y}$ is initially negative everywhere. The vorticity flux across the surface is

$$-\mu\frac{\partial \omega}{\partial y} = \frac{\partial p_\infty}{\partial x} + \frac{\partial u_w}{\partial t} + u_w\frac{\partial u_w}{\partial x} - v_w\omega\Big|_{y=0} \tag{1.1}$$

For a solid surface, the vorticity flux is determined by the pressure gradient, and $\dfrac{\partial \omega}{\partial y} < 0$ when the pressure gradient is positive (adverse). The initially negative vorticity is gradually cancelled out by this flux and a zero-vorticity line finally appears. Development of the boundary layer then comes to a new stage in which the zero-vorticity line plays an essential role. At this time, the flow begins to recirculate in certain regions and the shear stress is zero at points on the wall. Separation, however, does not occur at this stage. The boundary layer approximation is still valid and the displacement effect of the viscous layer on the outer inviscid flow is $O(Re^{-1/2})$.

At the second stage, the zero-vorticity line is elevated by convection. In the recirculation region, convection dominates diffusion and the flow is essentially inviscid. The momentum equation can be approximately written as

$$\frac{\partial u}{\partial t} + u\frac{\partial u}{\partial x} \approx 0 \tag{1.2}$$

which is a one-dimensional Burgers equation. In the inviscid flow, the zero-vorticity line corresponds to a material line. Fluid particles trapped on this line have different

speeds. At a finite time, particles on the line collide at a point, forming a singularity. A spike appears in the displacement thickness and the boundary layer equations break down. This is known as the Van Dommelen-Shen process (see Van Dommelen & Shen 1980,1982), and is characterized by increased thinning along the streamwise direction and thickening in the normal direction. The influence of the viscous effects are now much larger than $O(Re^{-1/2})$. A large amount of vorticity is shed into the outer flow over a very narrow region in the streamwise direction. Doligalski, Smith & Walker (1994) conjectured that the vorticity which erupts from the boundary layer rolls up into the primary stall vortex, leading to a series of complex phenomena.

One objective of the current research is to simulate unsteady boundary layer separation in a three-dimensional environment. As a helicopter blade usually has a large aspect ratio, and near the leading edge variations in the spanwise direction are smaller than streamwise variations, the three dimensional separation to a certain extent is similar to two-dimensional separation. The spanwise velocity has an influence on separation, but the effect is not large. However, the separation structure in three dimensions is more complex. For instance, in contrast to the two-dimensional case, the appearance of recirculating flow in a plane cut along any direction does not necessarily indicate separation. Since the vorticity now has two principal components $\omega_z \approx -\dfrac{\partial u}{\partial y}$ and $\omega_x \approx \dfrac{\partial w}{\partial y}$, separation is initiated on the zero-vorticity line associated with the intersection of the two iso-surfaces $\omega_x = 0$ and $\omega_z = 0$. Due to blade twist in flight, the angle of attack varies along the spanwise direction. The rotor trim scheme, the tip vortex, and the inboard trailing wake make the flow environment highly unsteady and simulation based on a comprehensive model is challenging. A trailing wake model can be constructed by extending the two-dimensional model of Zalutsky (2000) into three dimensions. In this model, a wake is shed from the trailing edge of a thin airfoil undergoing unsteady motions. The principle parameter is the strength of the wake vorticity $\gamma(t)$, which equals the tangential velocity jump at the trailing edge. γ satisfies an integral equation which can be solved once the temporal variation of the angle of attack is specified. Unsteady loads can then be evaluated. In three-dimensional flow, $\gamma = \gamma(z, t)$ also satisfies an integral equation (Katz & Plotkin 2001). For a helicopter with a high aspect-ratio blade, the integral equation can be solved in a much more efficient way by combining lifting line theory and the numerical procedures developed by Zalutsky (2000). Related asymptotic methods can be developed for rotating blades to find the leading order influence of the unsteady wake on leading edge separation.

For large aspect ratio wings, the separation process is quasi two-dimensional, and re-examination of two-dimensional results is very helpful. (More general three-dimensional separation structures were considered by Van Dommelen & Cowley (1990) Two-dimensional unsteady separation and control mechanisms are outlined in Chapter 2. Control studies for oscillating wings and for leading edge suction/injection are examined in detail. Results of the two-dimensional simulations are discussed in

Chapter 3. It is shown that there exists a band of frequences and amplitudes over which the separation time is significantly increased. Suction/injection calculations indicate that there can be an optimal location for the suction/injection slots that also increases the separation time. Unsteady three-dimensional boundary layer separation is discussed in Chapter 4. Both Eulerian and Lagrangian formulations are presented. Results of the three-dimensional computations are given in Chapter 5.

Chapter 2

Two-dimensional Unsteady Separation and Control

2.1 Introduction

As noted earlier, for helicopter blades with large aspect ratios, unsteady separation is quasi two-dimensional. Consequently, separation and control studies for two-dimensional flows provide useful guidance for prevention of three-dimensional separation on blades.

2.2 Unsteady separation without control

For an airfoil at incidence, because of a favorable pressure gradient, the velocity first accelerates along the upper surface. Leading edge curvature, however, varies in such a way that an adverse pressure gradient is encountered after a short distance. Within the boundary layer, fluid particles have a much smaller momentum compared with the outer flow, but have to overcome the same resistance due to the adverse pressure gradient. Beyond a critical incidence, boundary layer separation is expected. In unsteady flows, flow reversal or zero wall shear is no longer the defining characteristic for separation. A zero vorticity line, which appears in the recirculating flow, signals the onset of the Van Dommelen-Shen process (Van Dommelen & Shen 1980,1982). In a local zone, the boundary layer scale increases in the normal direction and shrinks in the streamwise direction. After a finite time, a singularity is generated by the collision of particles on the zero vorticity line and the subsequent boundary layer eruption ejects a large amount of vorticity into the outer layer. The boundary layer approximation then breaks down and a strong viscous/inviscid interaction associated with the next stage has to be described by another subset of the Navier-Stokes equations, Walker (2002).

Boundary layer separation initiates at the leading edge. Analyses within this

region are important for control studies. In notes by Van Dyke (1956), the airfoil leading edge zone is approximated by a parabola. Thin symmetric Joukowski airfoils provide a simple example. They are defined by

$$Y = \frac{4\varepsilon}{3\sqrt{3}}(1-X)\sqrt{1-X^2}, \tag{2.1}$$

where $X = -1$ is at the leading edge, $X = 1$ is at the trailing edge. ε denotes the thickness ratio of the airfoil, and $(X,\ Y)$ are dimensionless Cartesian coordinates with respect to the half-chord length $c/2$. The equation of a parabola with the same vertex point and dimensionless nose radius r_o is

$$Y = \sqrt{2r_o(X+1)}, \tag{2.2}$$

and $r_o = 64\varepsilon^2/27$ for the Joukowski airfoil defined in (2.1). Local coordinates near the nose may be recast, with repect to r_o, as

$$x = (X+1)/r_o, \qquad y = Y/r_o. \tag{2.3}$$

In the inviscid flow, the surface velocity on the parabola at incidence is given by Van Dyke (1956).

$$\frac{|q|}{A} = \left\{\frac{x}{x+1/2}\right\}^{1/2}\left\{1 \pm \frac{\alpha'}{\sqrt{x}}\right\}. \tag{2.4}$$

α' is proportional to the geometric incidence α (see 2.6 below). For a thin airfoil at incidence α, the velocity away from the leading edge is (Katz & Plotkin 2001)

$$\frac{q^*}{U_o} = 1 + \frac{4\epsilon}{\sqrt{3}}(1-2X) \pm \alpha\sqrt{\frac{1-X}{1+X}} \tag{2.5}$$

to first order. U_o is the uniform velocity in the free stream and α is the angle of attack. Matching with the velocity away from the leading edge gives

$$A = U_o\left(1 + \frac{4\epsilon}{\sqrt{3}}\right), \qquad \alpha' = \frac{3}{4}\sqrt{\frac{3}{2}}\frac{\alpha}{\epsilon}. \tag{2.6}$$

The invisid flow around the parabola is conveniently described in curvilinear coordinates. If the transformation

$$\begin{aligned} x &= \frac{1}{2}\left(\xi^2 - \eta^2 - 2\eta\right), \\ y &= \xi(\eta+1), \end{aligned} \tag{2.7}$$

is introduced, then the surface of the parabola becomes $\eta = 0$ and the coordinate ξ varies from $-\infty$ to ∞ on the surface of the parabola. A mapping between (x, y) and (ξ, η) is shown in Figure 2.1. The surface velocity around the leading edge is

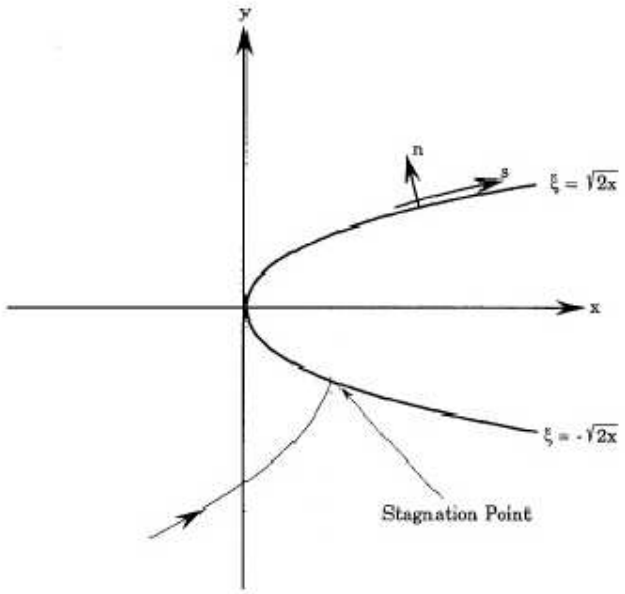

Figure 2.1: Parabolae of constant ξ and η, with the airfoil surface defined by $\eta = 0$

$$U_\infty(\xi, t) = \frac{\xi + \alpha_e}{\sqrt{\xi^2 + 1}}. \tag{2.8}$$

This result is consistent with (2.4) and α_e, defined as the effective angle of attack (see comments below 2.21,and also 2.41). When α_e is beyond a critical value, approximately 1.16, the boundary layer separates within a time $O(1)$, scaled using the local length r_o and velocity U_o. The streamwise position of the separation point is less than 2 on the upper surface of the parabola. This is relatively close to the leading edge vertex and similar results are expected for round-nosed airfoils.

The vector form of the non-dimensional Navier-Stokes equations for incompressible flow is

$$\frac{\partial \vec{\mathrm{v}}}{\partial \mathrm{t}} + \vec{\mathrm{v}} \times (\nabla \times \vec{\mathrm{v}}) + \frac{1}{2}\nabla(\vec{\mathrm{v}} \cdot \vec{\mathrm{v}}) = -\nabla \mathrm{p} - \frac{1}{\mathrm{Re}}\nabla \times (\nabla \times \vec{\mathrm{v}}), \tag{2.9}$$

$$\nabla \cdot \vec{\mathrm{v}} = 0. \tag{2.10}$$

General expressions for the vector operators in the curvilinear coordinates (ξ, η, ζ)

are

$$\nabla = \frac{1}{h_1}\frac{\partial}{\partial \xi}\vec{e}_1 + \frac{1}{h_2}\frac{\partial}{\partial \eta}\vec{e}_2 + \frac{1}{h_3}\frac{\partial}{\partial \zeta}\vec{e}_3,$$

$$\nabla \times \vec{\mathrm{v}} = \frac{1}{h_1 h_2 h_3}\begin{vmatrix} h_1\vec{e}_1 & h_2\vec{e}_2 & h_3\vec{e}_3 \\ \dfrac{\partial}{\partial xi} & \dfrac{\partial}{\partial \eta} & \dfrac{\partial}{\partial \zeta} \\ h_1 u_\xi & h_2 u_\eta & h_3 u_\zeta \end{vmatrix}, \tag{2.11}$$

where $\vec{e}_1$, $\vec{e}_2$ and $\vec{e}_3$ are the unit vectors in each of the coordinate directions and u_ξ, u_η and u_ζ are respective velocity components. In the normal direction, suitable scaled variables are

$$\tilde{v} = u_{\tilde{\eta}}\mathrm{Re}^{1/2}, \qquad Y = \tilde{\eta}\mathrm{Re}^{1/2}. \tag{2.12}$$

For the two-dimensional flow field, the momentum and continuity equations can be formulated in parabolic coordinates (ξ, η) as

$$\frac{\partial u_\xi}{\partial t} + \frac{1}{\sqrt{\xi^2+1}}\left(u_\xi\frac{\partial u_\xi}{\partial \xi} + u_\eta\frac{\partial u_\xi}{\partial \eta}\right) = -\frac{1}{\sqrt{\xi^2+1}}\frac{\partial p}{\partial \xi} + \frac{1}{\mathrm{Re}}\frac{1}{\xi^2+1}\frac{\partial^2 u_\xi}{\partial \eta^2}, \tag{2.13}$$

$$\frac{\partial p}{\partial \eta} = 0 \tag{2.14}$$

$$\frac{\partial u_\xi}{\partial \xi} + \frac{\partial u_\eta}{\partial \eta} + \frac{\xi u_\xi}{\xi^2+1} = 0. \tag{2.15}$$

Let u_ξ be written as u. New variables are introduced through

$$n = \mathrm{Re}^{1/2}\eta\sqrt{\tilde{\xi}^2+1}, \qquad s = \int_0^\xi \sqrt{r^2+1}\mathrm{d}r = \frac{1}{2}\left[\xi\sqrt{\xi^2+1} + \sinh^{-1}\xi\right], \tag{2.16}$$

$$v = u_\eta\mathrm{Re}^{1/2} + \frac{\xi\eta u\mathrm{Re}^{1/2}}{\xi^2+1} = u_\eta\mathrm{Re}^{1/2} + \frac{\xi n u}{\left(\tilde{\xi}^2+1\right)^{3/2}}. \tag{2.17}$$

In these variables, the familiar form of the boundary layer equations is restored, i.e.

$$\frac{\partial u}{\partial t} + u\frac{\partial u}{\partial s} + v\frac{\partial u}{\partial n} = -\frac{\partial p_\infty}{\partial s} + \frac{\partial^2 u}{\partial n^2}, \tag{2.18}$$

$$\frac{\partial u}{\partial s} + \frac{\partial v}{\partial n} = 0. \tag{2.19}$$

Corresponding boundary conditions are

$$u \to U_\infty = \frac{(\xi+\alpha_e)}{(\xi^2+1)^{1/2}} \ \ as \ \ n \to \infty; \qquad u = v = 0 \ \ at \ \ n = 0. \tag{2.20}$$

The pressure gradient in the momentum equation (2.18) is given by

$$-\frac{\partial p_\infty}{\partial s} = \frac{\partial U_\infty}{\partial t} + \frac{U_\infty}{\sqrt{\xi^2+1}}\frac{\partial U_\infty}{\partial \xi} = \frac{(\xi+\alpha_e)(1-\alpha_e\xi)}{(\xi^2+1)^{5/2}}, \tag{2.21}$$

The external velocity appears to depend only on the angle of attack α_e. This angle, however, is not merely the geometric angle of attack, but an effective angle of attack including effects from the airfoil geometry and unsteady motion. In the current approach, when the leading edge is approximated by a parabola, it is important for the inviscid flow calculation to evaluate the effective angle of attack α_e, see, e.g. Section 2.3.2. As the boundary layer nears separation, a region containing the zero-vorticity line thins as $(t_s - t)^{3/2}$ in the streamwise direction while the displacement thickness grows as $(t_s - t)^{-1/4}$ (Cowley & Van Dommelen 1990); t_s is the separation time. Eulerian calculations encounter great difficulty in revolving the associated large gradients in flow variables. Dynamically refined grids are not easy to implement since there is no clear feature in the Eulerian field that guides meshing. A Lagrangian approach seems to be the optimal adaptive scheme, and the variables (n and v) that become singular at separation do not appear in the governing equations. For various reasons, Lagrangian simulation is time consuming. It is convenient to switch from an Eulerian simulation to a Lagrangian one only at the final stage of the simulation. In the Lagrangian calculation, fluid particles are labeled by new coordinates ($\tilde{\xi}$,$\tilde{\eta}$). At the initial stage, they are specified as the physical positions of particles,

$$s(\tilde{\xi},\tilde{\eta},t_o) = \tilde{\xi}, \qquad n(\tilde{\xi},\tilde{\eta},t_o) = \tilde{\eta} \tag{2.22}$$

Subsequently, the two sets of coordinates are related by the Jacobian matrix,

$$J = \begin{pmatrix} \dfrac{\partial s}{\partial \tilde{\xi}} & \dfrac{\partial s}{\partial \tilde{\eta}} \\ \dfrac{\partial n}{\partial \tilde{\xi}} & \dfrac{\partial n}{\partial \tilde{\eta}} \end{pmatrix} \tag{2.23}$$

With the initial conditions (2.22), the continuity equation (2.19) is equivalent to the requirement that the determinant of the Jacobian matrix is unity, i.e.

$$\frac{\partial s}{\partial \tilde{\xi}}\frac{\partial n}{\partial \tilde{\eta}} - \frac{\partial s}{\partial \tilde{\eta}}\frac{\partial n}{\partial \tilde{\xi}} = 1. \tag{2.24}$$

The governing equations are now

$$\frac{\partial u}{\partial t} = -\frac{\partial P_\infty}{\partial s} + \frac{\partial^2 u}{\partial n^2}, \qquad \frac{\partial s}{\partial t} = u. \tag{2.25}$$

Derivatives with respect to n can be represented as

$$\frac{\partial}{\partial n} = \frac{\partial s}{\partial \tilde{\eta}}\frac{\partial}{\partial \tilde{\xi}} + \frac{\partial s}{\partial \tilde{\xi}}\frac{\partial}{\partial \tilde{\eta}} \tag{2.26}$$

which is then substituted into the momentum equation to give

$$\frac{\partial u}{\partial t} = -\frac{\partial P_\infty}{\partial s} + \Big\{ -\frac{\partial s}{\partial \tilde{\eta}}\frac{\partial}{\partial \tilde{\xi}} + \frac{\partial s}{\partial \tilde{\xi}}\frac{\partial}{\partial \tilde{\eta}} \Big\}^2 u, \tag{2.27}$$

with

$$\frac{\partial s}{\partial t} = u. \tag{2.28}$$

From the continuity equation (2.24), the normal position n of the particles is found by integration employing the method of characteristics. The continuity equation (2.24) has the charicteristic directions

$$\frac{\mathrm{d}\tilde{\xi}}{-\dfrac{\partial s}{\partial \tilde{\eta}}} = \frac{\mathrm{d}\tilde{\eta}}{\dfrac{\partial s}{\partial \tilde{\xi}}} = \frac{\mathrm{d}n}{1}. \tag{2.29}$$

$(\tilde{\xi}, \tilde{\eta})$ are interpreted as a line of initial locations of fluid particles arriving at constant s at a fixed time. n can therefore be obtained from

$$n(\tilde{\xi}, \tilde{\eta}, t) = \int_{\text{wall}}^{(\tilde{\xi},\tilde{\eta})} \frac{1}{\sqrt{s_{\tilde{\xi}}^2 + s_{\tilde{\eta}}^2}} \mathrm{d}s, \tag{2.30}$$

where partial derivatives $s_{\tilde{\xi}}$ and $s_{\tilde{\eta}}$ are evaluated at each time step.

A singularity occurs when a stationary point appears in the flow field, or equivalently,

$$\frac{\partial s}{\partial \tilde{\eta}} = 0, \qquad , \qquad \frac{\partial s}{\partial \tilde{\xi}} = 0. \tag{2.31}$$

As there are no singular variables in (2.27), Lagrangian simulations can go far beyond the separation time without convergence problems, although the governing equations are no longer valid because of the initiation of strong viscous/inviscid interaction. Nevertheless, Lagrangian calculations may encounter convergence issues. As the particles that were initially close to each other migrate apart, their physical positions can become increasingly distant from each other, and more iterations are needed at successive time steps. Because of this, a remesh procedure based on (2.24) is used when necessary.The singularity that the Lagrangian simulation detects may be a point of infinite displacement when the boundary layer separates, or a non-smooth behavior on a streamline. A discussion is presented in Chapter 3.

2.3 Boundary Layer Control

2.3.1 External Pressure Field Manipulation

For a thin airfoil undertaking an unsteady maneuver (see Figure 2.2), it is convenient to define the airfoil surface by writing

$$f = \pm\mu(x,t) + \nu(x,t) + g(x,t) \tag{2.32}$$

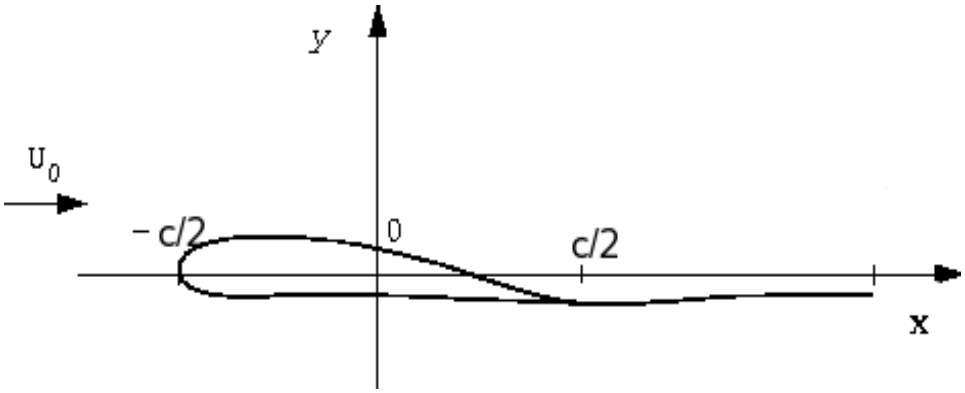

Figure 2.2: Schematic of an airfoil with wake

where $\mu(x,t)$ is the thickness or "fairing" distribution, $\nu(x,t)$ is the camber function, and $g(x,t)$ represents the unsteady maneuver. $'+'$ and $'-'$ denote upper and lower surfaces respectively. Temporal changes in μ represent a flexible surface. Similarly, temporal changes in ν can be used to describe airfoils with drooped leading edges, and even flexible surfaces. The time-dependent form g can allow unsteady maneuvers. In what follows, U_∞ is the free stream speed, c is the chord length, ϵ is the thickness/length ratio, $\alpha = O(\epsilon)$ is the angle of attack, and $\gamma(x,t)$ is the vorticity strength in the wake. The streamwise velocity for unsteady flow around the airfoil can be expanded as (Zalutsky 2000)

$$q = 1 + \epsilon q_1^{\pm} + \dots \tag{2.33}$$

where $\epsilon u_1^{\pm}$ is the first order perturbation, given by

$$\begin{aligned} q_1^{\pm} = &-\frac{1}{\pi}\int_{-1}^{1}\frac{\frac{\partial\mu}{\partial t}+\frac{\partial\mu}{\partial\xi}}{\xi-x}\,d\xi \pm \frac{1}{\pi}\sqrt{\frac{1-x}{1+x}}\int_{-1}^{1}\sqrt{\frac{1+\xi}{1-\xi}}\frac{-(\frac{\partial g}{\partial t}+\frac{\partial g}{\partial\xi}+\frac{\partial\nu}{\partial t}+\frac{\partial\nu}{\partial\xi})}{\xi-x}\,d\xi \\ &\pm \frac{1}{2\pi}\sqrt{\frac{1-x}{1+x}}\int_{1}^{1+t}\sqrt{\frac{\xi+1}{\xi-1}}\frac{\gamma(1+t-\xi)}{\xi-x}\,d\xi, \end{aligned} \tag{2.34}$$

This velocity is scaled with respect to U_∞ and the streamwise coordinates x and ξ with respect to c. Several application are discussed below.

2.3.2 Oscillating Wings

Oscillating wings are often used to study dynamic stall. For a rigid thin airfoil rotating around its center, the surface function is

$$f = \pm\mu(x) + \nu(x) - \alpha(t)x \tag{2.35}$$

The unsteady flow velocity on the surface of a thin airfoil is therefore,

$$\begin{aligned} q =& 1 + \epsilon q_1^{\pm} + \cdots \sim 1 + \epsilon \left\{ -\frac{1}{\pi}\int_{-1}^{1} \frac{\mu'(\xi)\,d\xi}{\xi+1} \right. \\ & \pm \sqrt{\frac{2}{1+x}} \int_{-1}^{1} \sqrt{\frac{1+\xi}{1-\xi}}\,(\dot{\alpha}\xi + \alpha(t))\,\frac{d\xi}{\xi+1} \\ & \left. \pm \frac{1}{2\pi}\sqrt{\frac{2}{1+x}} \int_{-1}^{1} \sqrt{\frac{1+\xi}{1-\xi}}\,\gamma(1+t-\xi)\,\frac{d\xi}{\xi+1} \right\}. \end{aligned} \tag{2.36}$$

In order to match the above expression with the leading edge velocity (2.4), a new scaled coordinate and scaled time

$$x = (X+1)/r_o, \quad T = \frac{t}{r_o/U_\infty}, \quad \text{with} \quad r_o = R_o\epsilon^2, \tag{2.37}$$

are introduced. Here r_o is the nose radius and $R_o = 64/27$ for the Joukowski airfoil (2.1). The dominant behavior of the surface velocity near the leading edge is,

$$q \sim 1 \pm \sqrt{\frac{2}{R_0 X}} \left\{ \int_{-1}^{1} \{\dot{\alpha}(t)\xi + \alpha(t)\}\ \frac{d\xi}{\sqrt{1-\xi^2}} + \frac{1}{2}\int_{1}^{1+t} \gamma(1+t-\xi)\,\frac{d\xi}{\sqrt{\xi^2-1}} \right\}, \tag{2.38}$$

Comparing this form with equation (2.4) shows that,

$$\alpha_e = \frac{2}{\pi\sqrt{R_0}} \left\{ \int_{-1}^{1} \{\dot{\alpha}(t)\xi + \alpha(t)\}\ \frac{d\xi}{\sqrt{1-\xi^2}} + \frac{1}{2}\int_{1}^{1+t} \gamma(1+t-\xi)\,\frac{d\xi}{\sqrt{\xi^2-1}} \right\}. \tag{2.39}$$

where α_e is an effective angle of attack and α is a geometric angle of attack. From the conservation of global circulation (Zalutsky 2002)

$$\begin{aligned} \Gamma_0 &= -2\int_{-1}^{1} \sqrt{\frac{1+\xi}{1-\xi}}(\alpha(t) + \dot{\alpha}(t)\,\xi)\,d\xi - \int_{1}^{1+t} \sqrt{\frac{\xi+1}{\xi-1}}\gamma(1+t-\xi)\,d\xi, \\ &= -2\int_{-1}^{1} \sqrt{\frac{1+\xi}{1-\xi}}(\alpha(t) + \dot{\alpha}(t)\,\xi)\,d\xi - \int_{1}^{1+t} \gamma(1+t-\xi)\,\frac{d\xi}{\sqrt{\xi^2-1}} + O(r_0^{\frac{3}{2}}) \end{aligned} \tag{2.40}$$

where Γ_0 is the global circulation around the wing and wake. Combining (2.40) and (2.39) leads to

$$\alpha_e(T) = -\frac{\Gamma_0}{2\pi} R_0^{-\frac{1}{2}} + R_0^{-\frac{1}{2}} \left\{ \alpha - \frac{1}{2r_o} \frac{d\alpha}{dT} \right\} + O(r_0^{\frac{3}{2}}). \tag{2.41}$$

For the situation when the airfoil oscillates harmonically around a constant angle α_o, with

$$\alpha(T) = R_0^{\frac{1}{2}} \left\{ \alpha_0 + r_0 \tilde{\alpha}_1 \left(1 - \cos \omega_0 T\right) \right\}, \tag{2.42}$$

the effective angle of attack is then

$$\alpha_e(T) = \alpha_0 - \frac{\tilde{\alpha}_1 \omega_0}{2} \sin \omega_0 T. \tag{2.43}$$

Eulerian and Lagrangian calculations results are discussed in Chapter 3.

2.3.3 Drooped Leading Edge

A drooped leading edge is rotated about the quarter-chord point of the airfoil. The geometric angle of attack is α and the drooping angle is β. The unsteady surface function is,

$$f = \begin{cases} \pm\mu(x) + \nu(x) - \alpha(t)x + \beta(t)(x + 1/2), & \text{for } x \le -1/2 \\ \pm\mu(x) + \nu(x) - \alpha(t)x, & \text{for } x > -1/2 \end{cases} \tag{2.44}$$

The horizontal surface velocity component is

$$\begin{aligned} q =& 1 + \epsilon q_1^{\pm} + \cdots \sim 1 + \epsilon \left\{ -\frac{1}{\pi} \int_{-1}^{1} \frac{\mu'(\xi)\, d\xi}{\xi + 1} \right. \\ & \pm \sqrt{\frac{2}{1+x}} \int_{-1}^{-1/2} \sqrt{\frac{1+\xi}{1-\xi}} \left(\dot{\alpha}\xi + \alpha(t) + \dot{\beta}\xi + \beta(t) \right) \frac{d\xi}{\xi + 1} \\ & \pm \sqrt{\frac{2}{1+x}} \int_{-1/2}^{1} \sqrt{\frac{1+\xi}{1-\xi}} \left(\dot{\alpha}\xi + \alpha(t) \right) \frac{d\xi}{\xi + 1} \\ & \left. \pm \frac{1}{2\pi} \sqrt{\frac{2}{1+x}} \int_{-1}^{1} \sqrt{\frac{1+\xi}{1-\xi}}\, \gamma(1 + t - \xi) \frac{d\xi}{\xi + 1} \right\}. \end{aligned} \tag{2.45}$$

Following the procedure sketched in (2.36)-(2.41), the effective angle of attack can be obtained as

$$\alpha_e(T) = -\frac{\Gamma_0}{2\pi} R_0^{-\frac{1}{2}} + R_0^{-\frac{1}{2}} \left\{ \alpha - \frac{1}{2r_o} \frac{d\alpha}{dT} + (\frac{1}{3} + \frac{\sqrt{3}}{2\pi})\beta - \frac{3\sqrt{3}}{8\pi r_o} \frac{d\beta}{dT} \right\} + O(r_0^{\frac{3}{2}}). \tag{2.46}$$

As an example, let α be fixed at α_0, and let the drooped nose oscillate around a constant angle β_0. The oscillation amplitude is $\tilde{\beta}_1$ and frequency is ω_0

$$\beta(T) = R_0^{\frac{1}{2}} \left\{ \beta_0 + r_0 \tilde{\beta}_1 \left(1 - \cos \omega_0 T\right) \right\}. \tag{2.47}$$

Thus

$$\alpha_e(T) = \alpha_0 + (\frac{1}{3} + \frac{\sqrt{3}}{2\pi})\beta_0 - \frac{3\sqrt{3}\tilde{\beta}_1\omega_0}{8\pi} \sin \omega_0 T. \tag{2.48}$$

This case is equivalent to the oscillating wing result (2.43), but with a higher α_0 and lower $\tilde{\alpha}_1$. Similarly, for a fixed drooped nose $\beta = \beta_0$ with the airfoil oscillating about the mid-chord point, from (2.46)

$$\alpha_e(T) = \alpha_0 + \beta_0 - \frac{\tilde{\alpha}_1\omega_0}{2} \sin \omega_0 T. \tag{2.49}$$

This case corresponds to a higher α_0 than (2.43). Based on the above discussion, separation on a maneuvering airfoil with a drooped nose can be studied as a special case of an oscillating airfoil.

2.3.4 Suction/Injection

Suppose that an injection slot is located on a section of the wall from C to D and a suction slot from A to B. This situation is sketched in Figure 2.3. The velocity

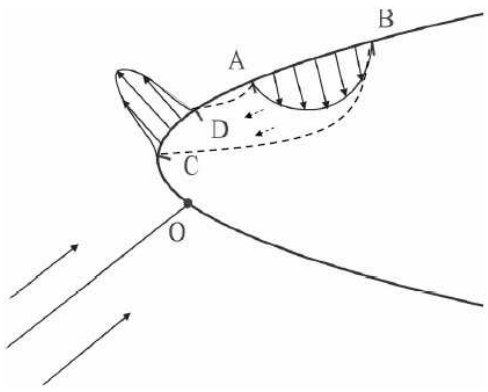

Figure 2.3: Schematic diagram of the passive device. The suction slot is between A and B while the injection slot is between C and D. Both the injection and suction are taken here to be normal to the surface.

distribution in the suction slot is taken as

$$v_s = -V_{w_s} \sin^n \left(\pi \frac{x - A}{B - A}\right), \tag{2.50}$$

while the velocity distribution in the injection slot is

$$v_i = V_{w_i} \sin^n \Big(\pi \frac{x - C}{D - C}\Big). \tag{2.51}$$

$n = 0$ corresponds to uniform suction and injection. $n = 3$, referred to as cubic suction and injection, can provide smooth influx into the boundary layer. The air flow rate in the suction slot should equal that of the injection slot. Thus

$$\int_C^D V_{w_i} \sin^n \Big(\pi \frac{x - C}{D - C}\Big) dx = \int_A^B V_{w_i} \sin^n \Big(\pi \frac{x - A}{B - A}\Big) dx, \tag{2.52}$$

which gives

$$V_{w_i} = V_{w_s} \Big(\frac{B - A}{D - C}\Big). \tag{2.53}$$

Over AB, the average pressure is higher than over CD; flow is ejected from AB to CD. When suction/injection is implemented on the surface of the parabola, the governing equations (2.18)-(2.19) do not change. For boundary conditions on the surface, the normal velocity component at suction/injection slots is given by (2.50) and (2.51) and is zero elsewhere.

Chapter 3

Two-dimensional Numerical Results

3.1 Oscillating Wings

Separation on oscillating wings is simulated at various frequencies, amplitudes and angles of attack. Without oscillation, the boundary layer separates when the scaled angle of attack is beyond a critical value 1.1556 (Werle & Davis 1972, Ruban 1981). However, the effective angle of attack during the oscillation involves both steady and time dependent terms. As shown in (2.43)

$$\alpha_e(T) = \alpha_0 - \frac{\tilde{\alpha}_1 \omega_0}{2} \sin \omega_0 T.$$

Clearly at high frequencies, the time dependent term has a significant effect. From Tables 3.1-3.4, it can be seen that the separation time varies considerably for oscillating wings. Previously, Zalutsky and Walker (2003) had suggested that at $\alpha_0 = 2.0, \tilde{\alpha}_1 = 1.0$, as ω_0 increases, the separation time first fluctuates around some value and then seems to blow up when $\omega_0 > 20$. Therefore extensive studies are carried out for various angles of attack with oscillation amplitudes from 0.25 to 4.0 and frequencies as high as 2000. Very small steps have to be used when the frequency becomes high. The following time steps are used in the simulation

$$dt = \begin{cases} 0.0005, & \omega_0 \leq 50 \\ 0.0002, & 50 < \omega_0 \leq 100 \\ 0.00002, & 100 < \omega_0 < 1000 \\ 0.00001, & 1000 \leq \omega_0 \end{cases} \tag{3.1}$$

At large frequencies, it may take several million steps for just one case before the simulation fails to converge. For $\alpha_0 = 4.0$, the proposed case studies are completed. The results are plotted in Figure 3.1. In Figure 3.1(a), for $\tilde{\alpha}_1 = 1.5$, the separation

time T increases monotonically. At $\omega_0 = 2000.0$, the boundary layer separates at $T = 8.46$, which is more than five times the non-oscillating value. In Figures 3.1(b)-(e), the separation time T first increases with ω_0 but then decays drastically after ω_0 exceeds a certain value. The spike, which corresponds to the maximum separation time T, occurs at lower frequencies as $\tilde{\alpha}_1$ increases. From Table 3.1, at $\alpha_0 = 4.0, \tilde{\alpha}_1 = 2.0$, the maximum separation time $T = 20.68$ when $\omega_0 = 700$. For $\tilde{\alpha}_1 = 1.5$, the maximum separation time $T = 90.09$ with $\omega_0 = 90$. It is interesting to note that T is very sensitive to both ω_0 and $\tilde{\alpha}_1$. After T reaches a maximum value, a small increase in ω_0 usually causes a substantial drop in T, as shown in Figure 3.1(e). The benefical effect of oscillation seems to occur only for $\tilde{\alpha}_1 < 1.5$. Further increases in $\tilde{\alpha}_1$ over most of the frequency spectrum, expediate separation. Spikes can also be seen in Figures 3.1(f)-(h),for $\tilde{\alpha}_1 > 1.5$. The computational results indicate that if an airfoil oscillates at a tuned frequency and amplitude, the separation time can be delayed by a factor of more than fifty, although the averaged angle of attack is high. In the simulation, ω_0 is scaled with respect to a reference value $1/t_o$, where (see 2.37)

$$t_o = \frac{r_o}{U_\infty}, \tag{3.2}$$

and its typical size is 10^{-4} for a rotating blade. In order for the oscillation to be effective, the actual frequency value should be as high as $10^5 \sim 10^6 s^{-1}$, which is too high for current engineering practice.

The streamline patterns near the leading edge at $\alpha_0 = 4.0, \tilde{\alpha}_1 = 1.5, \omega_0 = 2.0$ and $\alpha_0 = 4.0, \tilde{\alpha}_1 = 1.5, \omega_0 = 50$ are shown in Figures 3.2 and 3.3. By comparing these two figures, there are clearly two different mechanisms that lead to the failure of the simulations. In Figure 3.2(a),the low frequency case, streamlines bend slightly near the leading edge at time $t = 1$. From Figure 3.2(b), it can be seen that a bubble, or flow recirculation, forms on the upper surface and the skewing of streamlines becomes pronounced. In Figure 3.2(c), the bubble is stretched along a line across which streamlines become discontineous. The boundary layer has separated and large fluctuactions in the streamline patterns are observed. For this low frequency case, separation is initiated by the appearance of a zero-vorticity line and culminates in the vorticity spike. The high frequency case is different. In Figure 3.3(a), an elongated bubble can be seen on the surface at $t = 1$. Due to the motion of the oscillating airfoil, streamlines are no longer smooth, but small amplitude oscillations appear on streamlines upstream of the leading edge. The bubble disappears in successive steps, as seen in Figures 3.3 (b)-(d), and the fluctuation amplitudes on the streamline patterns decay. At $t = 10$ in Figure 3.3(e), a discontinuity appears on the streamlines and its position should correspond to the maximum and minimun of the oscillation angles. In Figure 3.3 (f), when $t = 12$, streamlines are substantially perturbed by the airfoil maneuvers. In Figure 3.3 (g), a large oscillation is seen in the flow patterns and the boundary layer separates at $t = 13.97$. Notice that for this case, flow reversal is no longer seen after $t = 1$ and the simulation diverges because

the flow field is subject to very strong disturbances over a long time.

Lagrangian methods were used for both low frequency and high frequency cases. At low frequencies, $\omega_0 = 2.0$, both Lagrangian and Eulerian results agree and give a separation time around $T = 2.6$. For the high frequency case with $\omega_0 = 50.0$, the Lagrangian calculations initiated at different starting times quickly terminate. The Eulerian calculations suggest $T = 13.9$. It is conjectured that Lagrangian simulations are very sensitive to high frequency irregularities that occur on the steamlines.

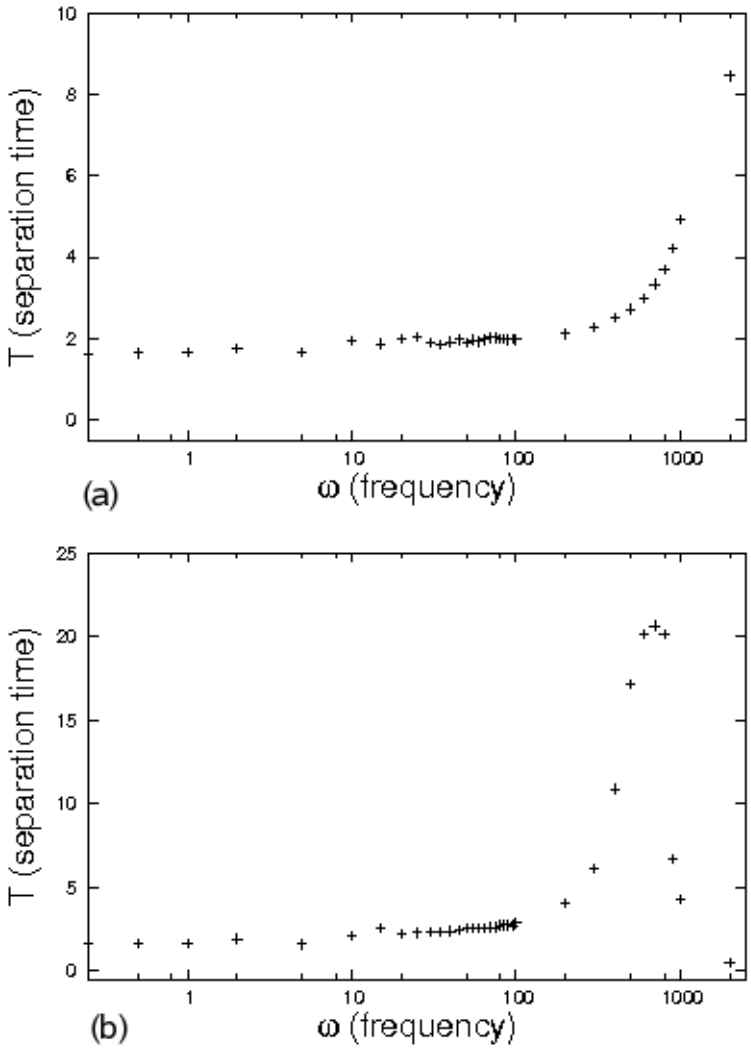

Figure 3.1: Separation times for an oscillating wing at various frequencies and amplitudes. Averaged angle of attack $\alpha_0 = 4.0$, and oscillation amplitudes (a) $\tilde{\alpha}_1 = 0.25$, (b) $\tilde{\alpha}_1 = 2.0$

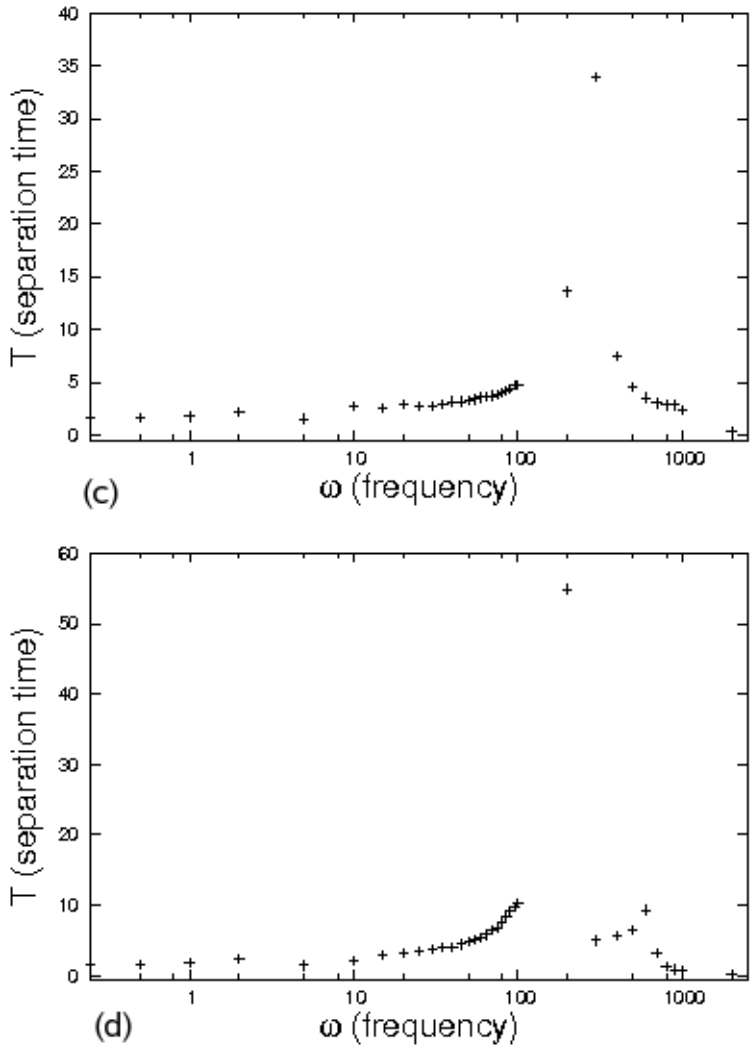

Figure 3.1: Separation times for an oscillating wing at various frequencies and amplitudes. Averaged angle of attack $\alpha_0 = 4.0$, and oscillation amplitudes (c) $\tilde{\alpha}_1 = 0.75$, (d) $\tilde{\alpha}_1 = 1.0$

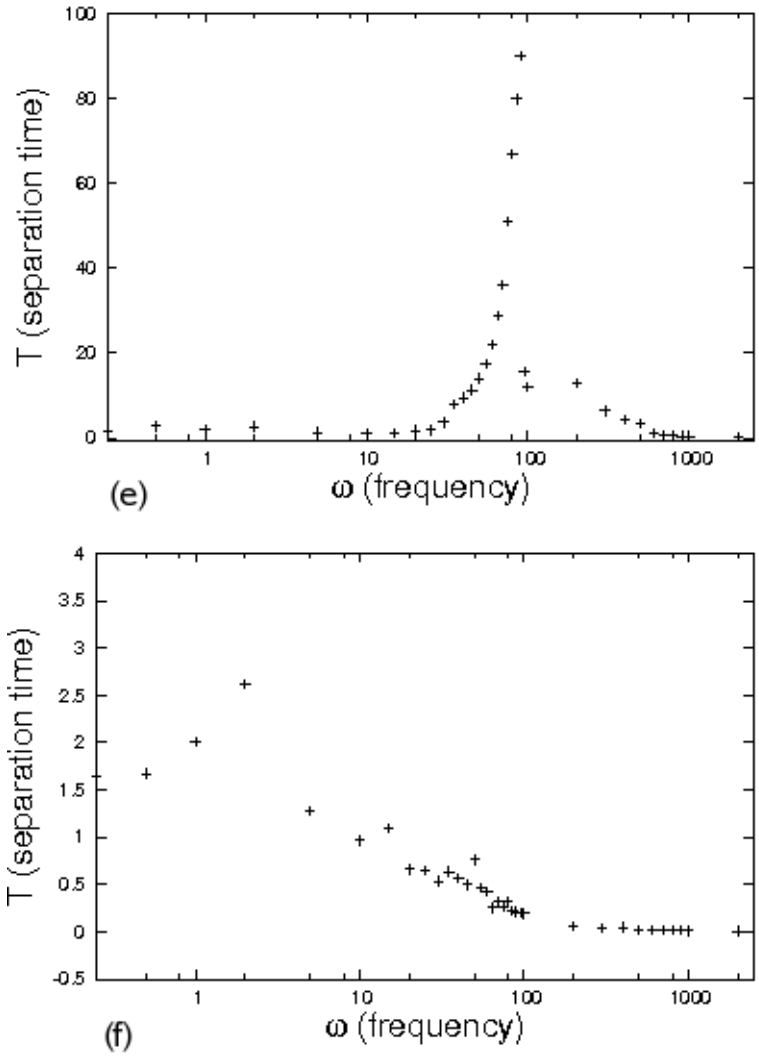

Figure 3.1: Separation times for an oscillating wing at various frequencies and amplitudes. Averaged angle of attack $\alpha_0 = 4.0$, and oscillation amplitudes (e) $\tilde{\alpha}_1 = 1.5$, (f) $\tilde{\alpha}_1 = 2.0$

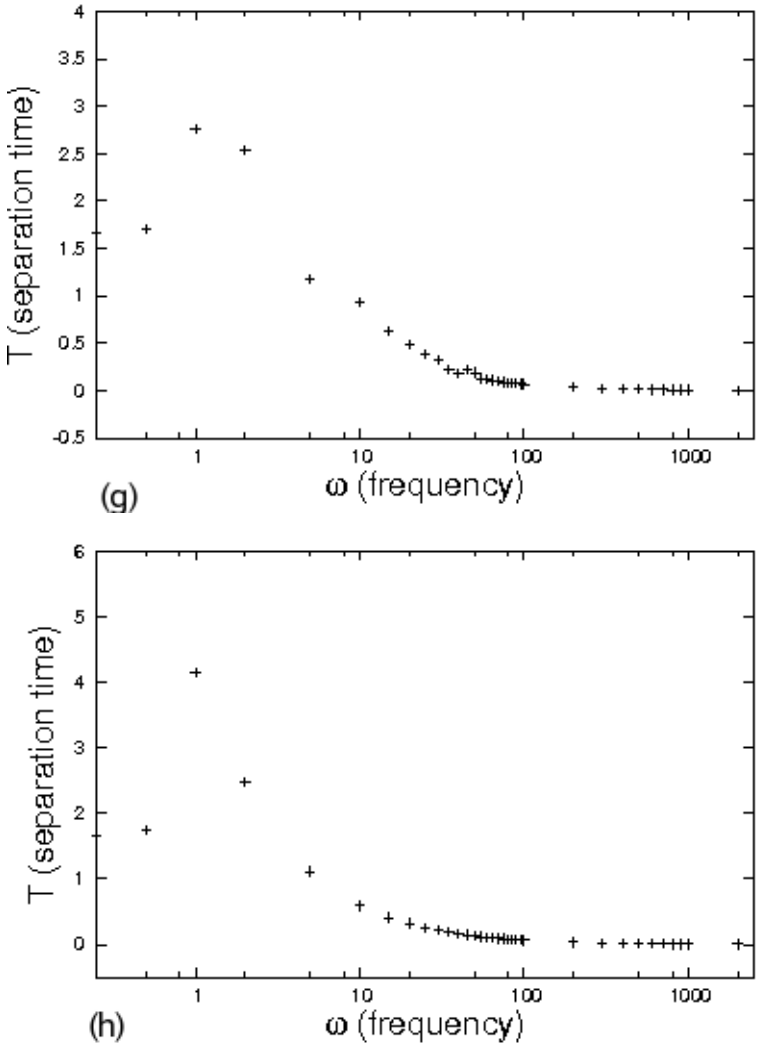

Figure 3.1: Separation times for an oscillating wing at various frequencies and amplitudes. Averaged angle of attack $\alpha_0 = 4.0$, and oscillation amplitudes (g) $\tilde{\alpha}_1 = 3.0$, (h) $\tilde{\alpha}_1 = 4.0$

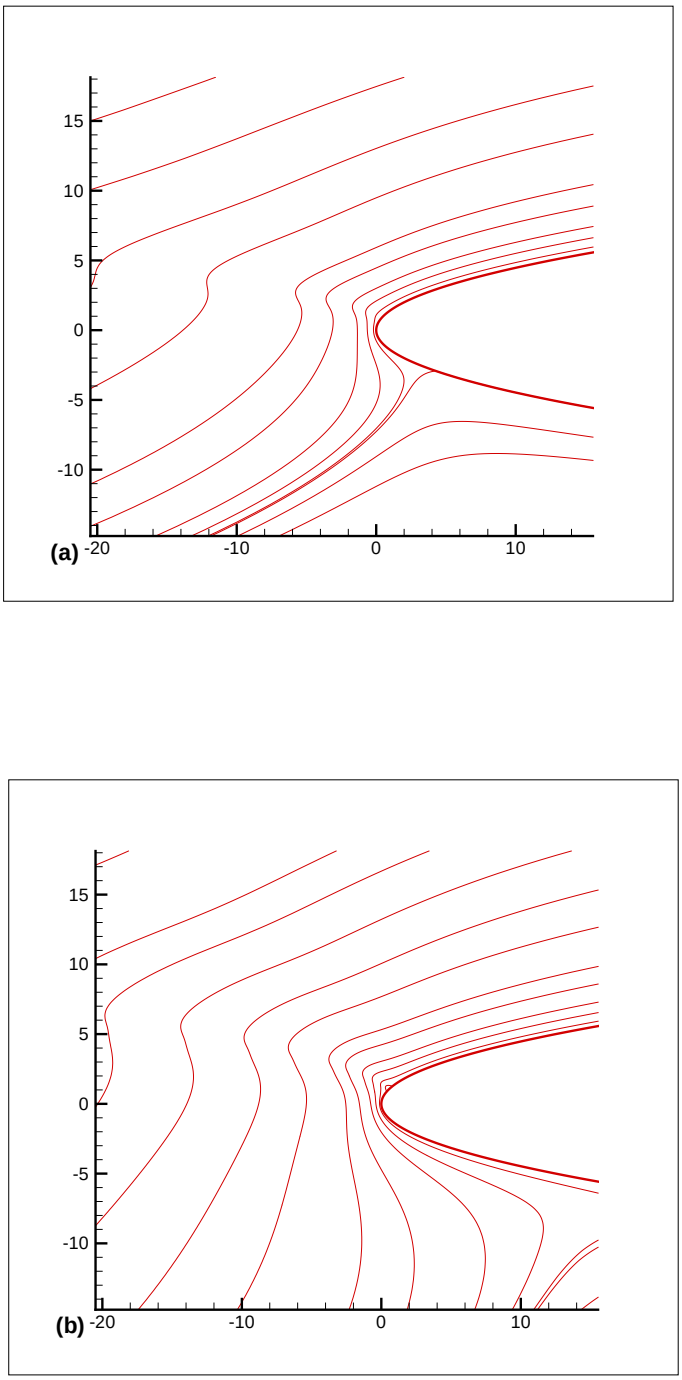

Figure 3.2: Temporal development of the instantaneous streamlines for $\alpha_0 = 4.0$, $\tilde{\alpha}_1 = 1.5$, and $\omega = 2.0$ in physical coordinates (x, y) at times (a) t=1.0, (b) t=2.0

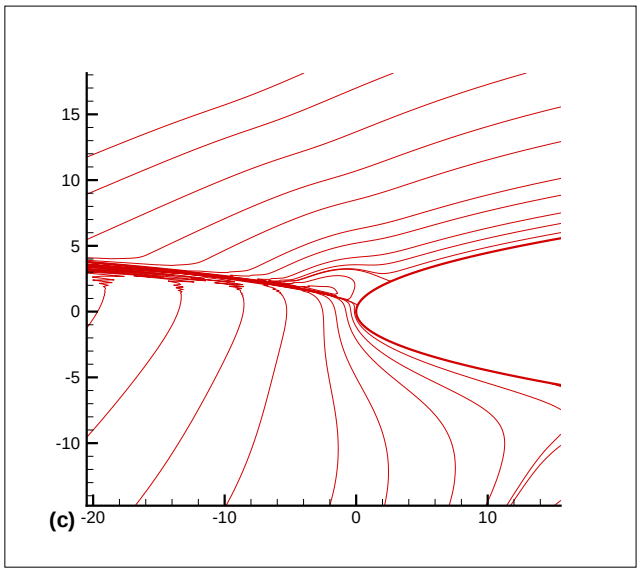

Figure 3.2: Temporal development of the instantaneous streamlines for $\alpha_0 = 4.0$, $\tilde{\alpha}_1 = 1.5$, and $\omega = 2.0$ in physical coordinates (x, y) at the time (c) t=2.739

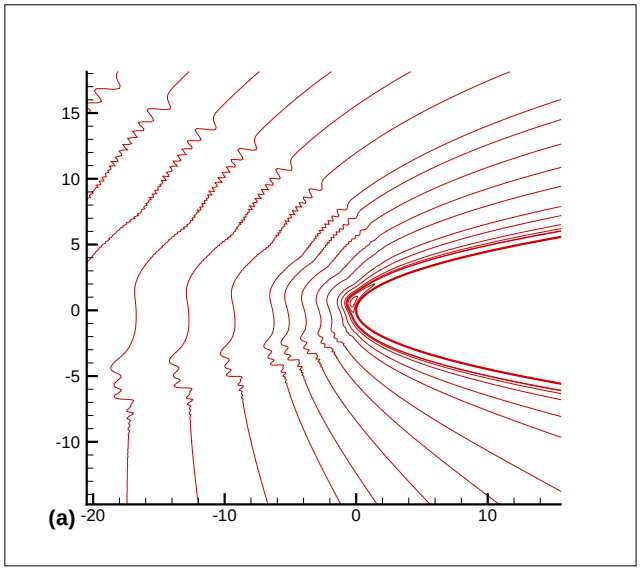

Figure 3.3: Temporal development of the instantaneous streamlines for $\alpha_0 = 4.0$, $\tilde{\alpha}_1 = 1.5$, and $\omega = 50.0$ in physical coordinates (x, y) at the time (a) t=1.0

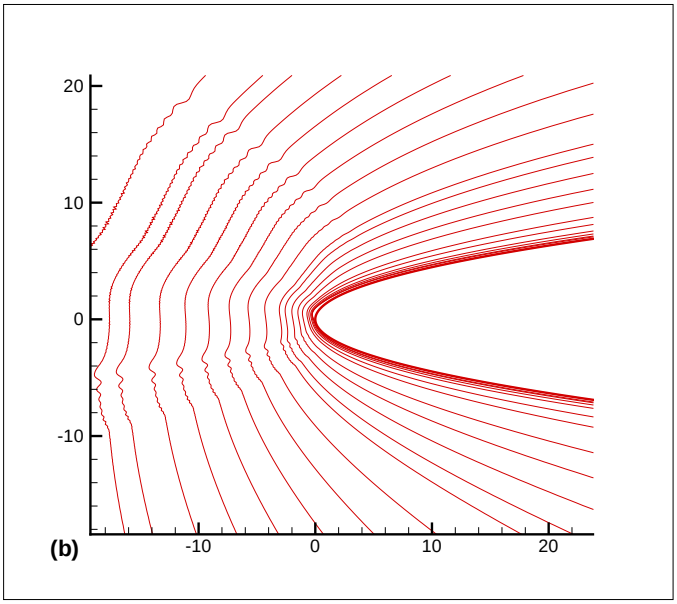

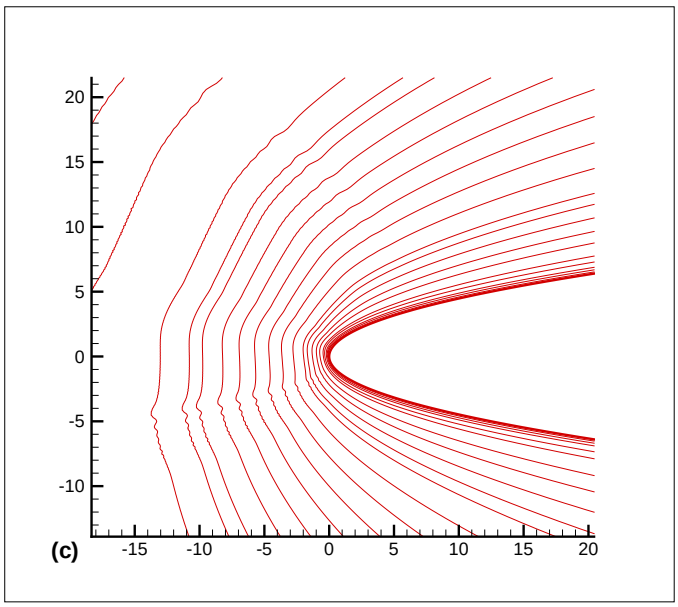

Figure 3.3: Temporal development of the instantaneous streamlines for $\alpha_0 = 4.0$, $\tilde{\alpha}_1 = 1.5$, and $\omega = 50.0$ in physical coordinates (x, y) at the time (b) t=2.0, (c) t=3.0

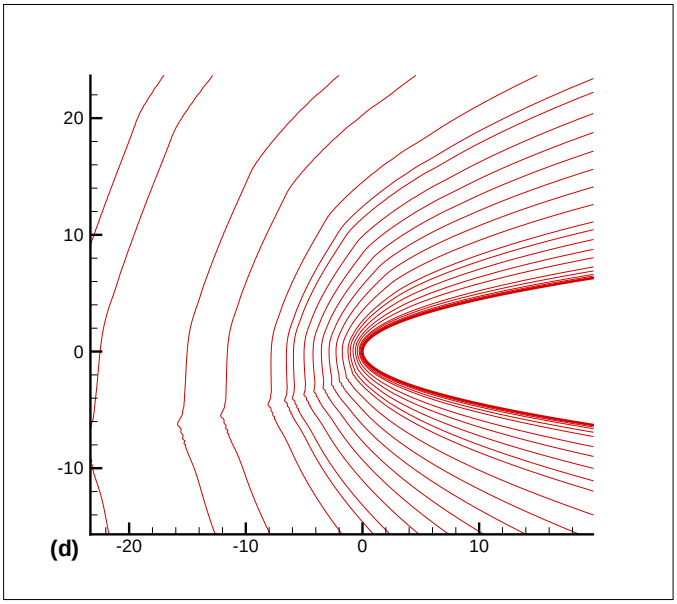

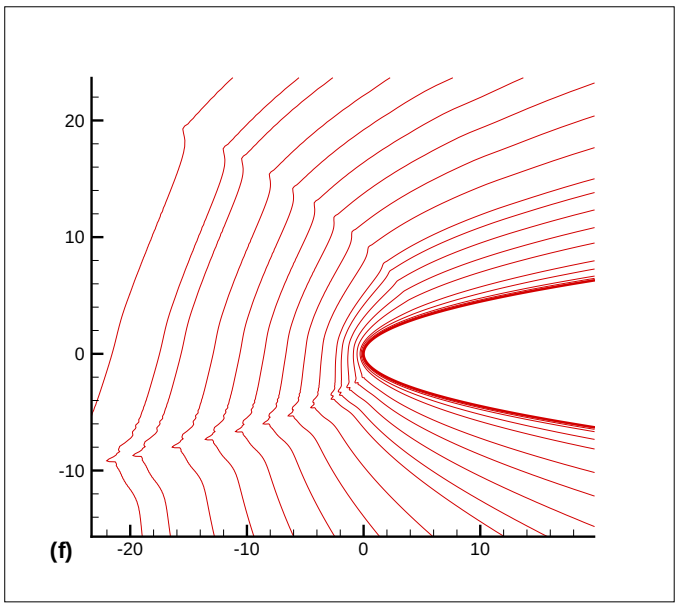

Figure 3.3: Temporal development of the instantaneous streamlines for $\alpha_0 = 4.0$, $\tilde{\alpha}_1 = 1.5$, and $\omega = 50.0$ in physical coordinates (x, y) at the time (d) t=6.0, (e) t=10.0

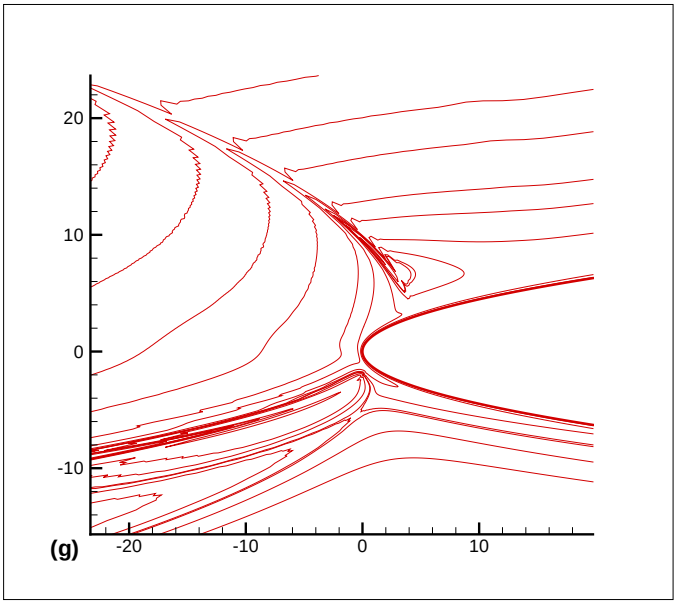

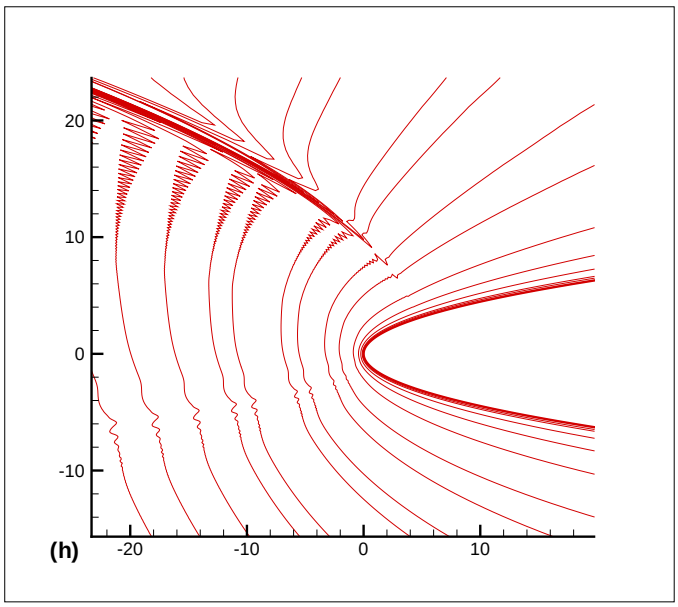

Figure 3.3: Temporal development of the instantaneous streamlines for $\alpha_0 = 4.0$, $\tilde{\alpha}_1 = 1.5$, and $\omega = 50.0$ in physical coordinates (x, y) at the time (f) t=12.0, (g) t=13.97

$\alpha_0 = 4.0$	$\tilde{\alpha}_1 \rightarrow$	0.25	0.50	0.75	1.0	1.5	2.0	3.0	4.0
$\omega_0 \downarrow$									
0.25		1.630	1.632	1.634	1.637	1.642	1.647	1.657	1.668
0.5		1.637	1.648	1.659	1.670	1.674	1.674	1.702	1.739
1		1.656	1.674	1.722	1.774	1.872	2.011	2.766	4.153
2		1.768	1.917	2.146	2.385	2.636	2.620	2.538	2.472
5		1.654	1.600	1.522	1.463	1.364	1.280	1.745	1.110
10		1.937	2.138	2.718	2.117	0.969	0.965	0.939	0.589
15		1.871	2.526	2.611	3.030	1.084	1.096	0.632	0.410
20		1.99	2.227	2.848	3.162	1.741	0.662	0.490	0.324
25		2.027	2.279	2.779	3.527	1.897	0.645	0.386	0.258
30		1.906	2.318	2.767	3.792	3.646	0.538	0.322	0.216
35		1.846	2.351	2.910	3.969	7.934	0.639	0.223	0.184
40		1.917	2.386	3.158	4.115	9.455	0.562	0.180	0.161
45		1.969	2.419	3.155	4.489	11.33	0.500	0.219	0.144
50		1.911	2.529	3.287	4.798	13.97	0.765	0.191	0.129
55		1.959	2.531	3.373	5.146	17.45	0.468	0.129	0.116
60		1.928	2.531	3.571	5.359	22.03	0.427	0.121	0.106
65		1.969	2.563	3.601	5.805	28.83	0.254	0.107	0.099
70		2.023	2.616	3.701	6.555	36.15	0.318	0.100	0.092
75		2.024	2.611	3.870	6.819	51.08	0.258	0.091	0.085
80		1.992	2.716	4.020	7.685	66.94	0.320	0.087	0.080
85		2.007	2.738	4.154	8.404	79.87	0.226	0.080	0.075
90		1.976	2.732	4.337	9.197	90.09	0.212	0.079	0.071
95		2.001	2.728	4.702	9.768	15.72	0.203	0.071	0.068
100		1.974	2.858	4.723	10.32	12.07	0.194	0.069	0.064
200		2.117	4.064	13.60	54.90	13.01	0.064	0.035	0.032
300		2.284	6.145	33.97	5.024	6.432	0.044	0.023	0.021
400		2.514	10.89	7.457	5.696	4.334	0.048	0.017	0.016
500		2.723	17.17	4.592	6.526	3.380	0.026	0.014	0.013
600		2.981	20.16	3.509	9.326	1.268	0.022	0.011	0.011
700		3.341	20.68	3.019	3.290	0.683	0.019	0.010	0.009
800		3.705	20.19	2.834	1.340	0.519	0.017	0.009	0.008
900		4.213	6.697	2.807	0.873	0.385	0.015	0.008	0.007
1000		4.934	4.283	2.401	0.780	0.384	0.013	0.007	0.006
2000		8.464	0.522	0.341	0.253	0.186	0.006	0.003	0.003

Table 3.1: Calculated results for the separation time T_s and separation location $s_s, \hat{s}_s$

.

$\alpha_0 = 3.0$	$\tilde{\alpha}_1 \rightarrow$	0.25	0.50	0.75	1.0	1.5	2.0	3.0	4.0
$\omega_0 \downarrow$									
0.25		2.539	2.550	2.561	2.573	2.600	2.631	2.621	2.648
0.5		2.576	2.640	2.618	2.656	2.739	2.836	3.021	3.377
1		2.682	2.808	3.008	3.272	3.976	4.848	4.814	4.740
2		2.876	3.154	3.207	3.157	3.021	2.921	2.749	2.637
5		2.704	2.870	4.004	1.707	1.809	1.825	1.239	1.149
10		2.887	3.902	4.412	5.044	2.250	1.014	0.944	0.605
15		3.142	3.460	4.208	5.082	8.004	1.083	0.673	0.434
20		2.979	3.486	4.423	5.414	5.516	0.804	0.479	0.323
25		3.059	3.557	4.584	6.058	11.61	1.022	0.297	0.255
30		2.972	3.610	4.841	6.516	14.71	0.862	0.236	0.215
35		3.104	3.817	4.893	7.105	18.78	1.099	0.199	0.183
40		3.046	3.836	5.212	7.613	24.31	1.033	0.173	0.161
45		2.995	3.813	5.349	8.546	32.08	0.912	0.153	0.143
50		3.049	3.932	5.557	9.200	47.11	0.644	0.138	0.129
55		3.014	4.026	5.851	10.10	71.15	0.408	0.135	0.116
60		3.065	4.034	6.297	11.22	100.6	0.428	0.119	0.107
65		3.108	4.168	6.494	12.77	122.2	0.299	0.107	0.099
70		3.077	4.236	6.837	14.21	136.4	0.275	0.101	0.091
75		3.142	4.268	7.226	16.63	146.6	0.256	0.092	0.085
80		3.095	4.487	7.638	17.96	153.0	0.240	0.085	0.080
85		3.064	4.590	8.145	20.13	157.3	0.225	0.083	0.075
90		3.152	4.659	8.829	22.82	158.8	0.179	0.076	0.071
95		3.127	4.716	9.075	26.42	153.3	0.169	0.074	0.067
100		3.103	4.786	9.821	31.35		0.160	0.068	0.064
200		3.473	7.923	42.64	80.09		0.064	0.035	0.032
300		3.878	16.03	51.49			0.043	0.023	0.021
400		4.245	26.85	44.45			0.032	0.017	0.016
500		4.892	29.45				0.026	0.014	0.013
600		5.841	28.50				0.022	0.011	0.011
700		6.928	26.33				0.019	0.010	0.009
800		8.066	23.37				0.016	0.009	0.008
900		9.269					0.014	0.008	0.007
1000		11.16					0.013	0.007	0.006
2000		1.907					0.006	0.003	0.003

Table 3.2: Calculated results for the separation time T_s and separation location $s_s, \hat{s}_s$

.

$\alpha_0 = 2.0$	$\tilde{\alpha}_1 \rightarrow$	0.25	0.50	0.75	1.0	1.5	2.0	3.0	4.0
$\omega_0 \downarrow$									
0.25		5.825	6.004	6.019	6.210	6.372	6.940	7.903	10.12
0.5		6.158	6.539	7.083	7.629	9.511	10.20	9.983	9.75
1		6.420	6.927	6.846	6.637	6.303	6.015	5.610	5.338
2		6.108	6.380	6.650	4.091	3.596	3.330	3.015	2.829
5		6.653	8.050	10.352	11.38	15.20	20.26	1.883	1.199
10		7.005	8.239	9.479	11.42	18.26	1.619	1.632	0.650
15		6.762	8.013	10.185	12.69	24.86	1.540	0.655	0.430
20		6.650	8.000	10.52	14.52	35.67	1.910	0.375	0.322
25		6.629	8.345	11.35	16.16	53.00	1.640	0.307	0.257
30		6.742	8.451	11.98	18.92	96.74	1.170	0.235	0.214
35		6.721	8.822	12.97	21.78	180.0	0.995	0.201	0.184
40		6.786	8.985	13.59	26.04	228.5	1.582	0.240	0.162
45		6.760	9.246	14.74	31.21	252.3	1.265	0.157	0.144
50		6.814	9.327	16.54	36.89	262.3	0.398	0.137	0.129
55		6.796	9.628	18.26	46.35	271.3	0.357	0.126	0.116
60		6.843	10.07	19.31	61.41	264.6	0.424	0.117	0.107
65		6.881	10.63	21.30	81.75		0.294	0.109	0.098
70		6.865	10.63	23.73	99.04		0.189	0.098	0.092
75		6.891	10.99	26.13	112.6		0.213	0.096	0.085
80		6.928	11.41	28.59	121.7		0.164	0.085	0.080
85		6.979	11.84	32.21	128.0		0.152	0.083	0.075
90		7.169	12.24	36.80	132.6		0.144	0.075	0.071
95		7.164	12.65	41.99	135.4		0.137	0.072	0.068
100		7.145	13.21	48.50	136.4		0.131	0.068	0.064
200		8.248		87.83	91.08		0.066	0.035	0.031
300		9.852			91.08		0.043	0.023	0.021
400		12.33			64.46		0.032	0.018	0.016
500		16.49					0.026	0.014	0.013
600		20.84			3.620		0.022	0.011	0.011
700		22.98			1.268		0.019	0.010	0.009
800		23.62			0.890		0.016	0.009	0.008
900		24.05			0.723		0.014	0.008	0.007
1000					0.597		0.013	0.007	0.006
2000					0.233		0.006	0.003	0.003

Table 3.3: Calculated results for the separation time T_s and separation location $s_s, \hat{s}_s$

.

$\alpha_0 = 1.5$	$\tilde{\alpha}_1 \rightarrow$	0.25	0.50	0.75	1.0	1.5	2.0	3.0	4.0
$\omega_0 \downarrow$									
0.25		15.23	16.71	18.07	20.06	22.29	21.97	21.13	20.48
0.5		15.47	15.97	15.40	14.94	13.52	12.74	11.68	11.05
1		14.37	14.08	14.23	14.40	7.69	6.914	6.155	5.742
2		15.32	16.63	19.69	22.97	4.19	42.75	3.212	2.957
5		16.97	20.30	22.73	26.63	42.02	74.95	3.189	1.240
10		16.44	19.59	24.16	31.65	72.54	3.487	0.975	0.653
15		16.04	19.83	26.17	38.22	221.2	1.944	0.651	0.430
20		16.40	20.29	28.75	49.20	446.5	5.831	0.375	0.319
25		16.64	21.21	33.04	65.72	473.2	4.912	0.284	0.257
30		16.21	21.85	37.43	96.83	483.4	3.778	0.235	0.214
35		16.24	22.71	43.03	167.19	438.3	1.091	0.200	0.183
40		16.28	23.93	50.31	212.96	404.7	0.642	0.175	0.160
45		16.43	25.38	58.89	238.72	377.6	1.546	0.151	0.143
50		16.55	26.17	73.94	247.52	360.9	0.387	0.138	0.129
55		16.80	28.27	96.03	258.24	356.6	0.239	0.127	0.115
60		16.92	29.81	120.3	254.9		0.220	0.117	0.106
65		17.05	31.55	137.0			0.295	0.116	0.098
70		17.15	32.23	148.2			0.186	0.097	0.091
75		17.28	35.42	155.9		295.4	0.173	0.092	0.085
80		17.43	39.02	160.2			0.163	0.087	0.080
85		17.65	40.53	162.9			0.154	0.080	0.075
90		17.98	42.77	164.3			0.150	0.077	0.071
95		18.10	47.34	163.3			0.208	0.072	0.067
100		18.15	53.33	161.6		234.0	0.163	0.068	0.064
200		23.13					0.066	0.035	0.031
300		34.39					0.043	0.023	0.021
400		45.40					0.032	0.018	0.016
500				18.12		0.805	0.0260	0.014	0.013
600				2.383		0.776	0.022	0.012	0.011
700				1.338		0.620	0.019	0.010	0.009
800				0.947		0.527	0.016	0.009	0.008
900				0.866		0.433	0.014	0.008	0.007
1000				0.868		0.409	0.013	0.007	0.006
2000				0.310		0.154	0.006	0.003	0.003

Table 3.4: Calculated results for the separation time T_s and separation location $s_s, \hat{s}_s$

.

3.2 Suction/Injection

Table 3.5 (a),(b) show calculated separation times for uniform suction/injection. The distances of the slot locations from the leading edge vertex are measured using (2.16). From the tables, it can be seen that increasing the injection/suction strength can initially delay separation. As the injection strength increases further, the separation time decreases and can become smaller than the no-control value of 5.8. The locations of the suction/injection slots can also have a considerable effect on separation. In particular, there are optimal locations for leading edge suction slots that almost double the no-control value of the separation time (see Tables 3.5 a,b).

		V_w	0.1	0.2	0.5	1.0
CD	AB					
(0.05,0.4)	(0.5,1.5)		5.812	5.867	6.202	6.643
(0,0.3)	(0.5,2)		6.623	7.071	7.011	7.871
(0.1,0.4)	(0.5,2)		6.57	7.069	7.063	7.875
(0,0.4)	(0.5,2)		6.594	7.091	7.135	7.803
(-0.1,0.4)	(0.5,2)		6.627	7.052	7.009	7.772
(-0.2,0.4)	(0.5,2)		6.663	7.032	7.059	7.967
(0,0.4)	(0.5,2.5)		6.511	7.672	8.842	9.213
(-0.1,0.4)	(0.5,2.5)		6.567	7.742	8.744	9.664
(0.05,0.35)	(0.5,2.5)		6.512	7.67	8.847	7.299
(-0.2,0.4)	(0.5,2.5)		6.635	7.821	8.796	9.549
(0,0.3)	(0.5,3)		6.211	6.705	7.652	5.213
(0,0.4)	(0.5,3)		6.175	6.708	7.213	5.39
(-0.1,0.4)	(0.5,3)		6.218	6.699	7.797	6.116
(-0.25,0.4)	(0.5,3)		6.279	6.827	8.572	6.89
(0.05,0.35)	(0.5,3.5)		6.012	6.122	5.993	4.383
(0,0.4)	(0.5,3.5)		6.012	6.121	6.032	4.711
(-0.15,0.35)	(0.5,3.5)		6.159	6.256	6.317	5.288
(-0.3,0.4)	(0.5,3.5)		6.018	6.321	6.653	5.826

Table 3.5: (a) Calculated separation time for suction/injection at an angle of attack $\alpha_e = 2.0$

		V_w	1.5	2.0	3.0	5.0
CD	AB					
(0.05,0.4)	(0.5,1.5)		7.229	7.849	8.741	4.656
(0,0.3)	(0.5,2)		9.155	5.666	4.282	1.26
(0.1,0.4)	(0.5,2)		5.428	4.209	3.713	1.012
(0,0.4)	(0.5,2)		8.938	5.415	4.035	2.719
(-0.1,0.4)	(0.5,2)		8.831	9.755	4.599	3.959
(-0.2,0.4)	(0.5,2)		8.908	9.888	7.044	4.411
(0,0.4)	(0.5,2.5)		4.793	4.144	3.735	1.022
(-0.1,0.4)	(0.5,2.5)		6.159	4.523	4.0	3.642
(0.05,0.35)	(0.5,2.5)		4.536	4.025	2.526	0.786
(-0.2,0.4)	(0.5,2.5)		11.148	5.469	3.868	3.814
(0,0.3)	(0.5,3)		4.162	3.844	1.326	0.712
(0,0.4)	(0.5,3)		4.126	3.769	3.18	0.811
(-0.1,0.4)	(0.5,3)		4.575	4.055	3.691	1.26
(-0.25,0.4)	(0.5,3)		5.137	4.404	3.868	2.507
(0.05,0.35)	(0.5,3.5)		3.786	2.835	0.81	0.682
(0,0.4)	(0.5,3.5)		3.869	3.703	1.224	0.654
(-0.15,0.35)	(0.5,3.5)		4.335	3.942	3.688	1.134
(-0.3,0.4)	(0.5,3.5)		4.796	4.178	3.788	3.603

Table 3.5: (b) Calculated separation time for suction/injection at an angle of attack $\alpha_e = 2.0$

Chapter 4

Three-Dimensional Boundary Layer Separation

4.1 Introduction

Two different helicopter flight conditions are considered for the three-dimensional boundary layer separation studies: hovering and forward flight. During a hovering flight, in a frame fixed with the rotating blade, the oncoming velocity

$$U_o = \Omega r \tag{4.1}$$

in the streamwise direction is time independent. The lifting blade at incidence can be represented by a suitable surface vorticity distribution or bound circulation. According to Kelvin's theorem, variation of the bound circulation leads to the shedding of an inboard vortex sheet from the trailing edge. At the blade tip, the bound circulation rolls up into a tip vortex causing considerable downwash in this region. In industry a cut-off parameter is often used near the blade tip when calculating the thrust coefficient (Leishman 2000) because of the low effective angle of attack due to the influence of the tip vortex. Unlike trailing wakes from a fixed wing, which move away after shedding, trailing wakes (including the inboard vortex sheet and the tip vortex) for a hovering rotorcraft remain beneath the blades and impose a much larger effect. The downwash induced by trailing wakes is discussed in Appendix A. Forward flight is a more complex situation. As the helicopter has a forward speed, the oncoming velocity with respect to the blade is different at various azimuthal locations (shown in Figure 4.1). An advancing blade with a 90° azimuthal angle experiences the highest oncoming velocity while a retreating blade with a 270° azimuthal angle encounters the lowest oncoming velocity. The oncoming velocity can be written as

$$U_o = \Omega r + \mu sin(\Psi_0 + \Omega t), \tag{4.2}$$

$$W_o = \mu cos(\Psi_0 + \Omega t). \tag{4.3}$$

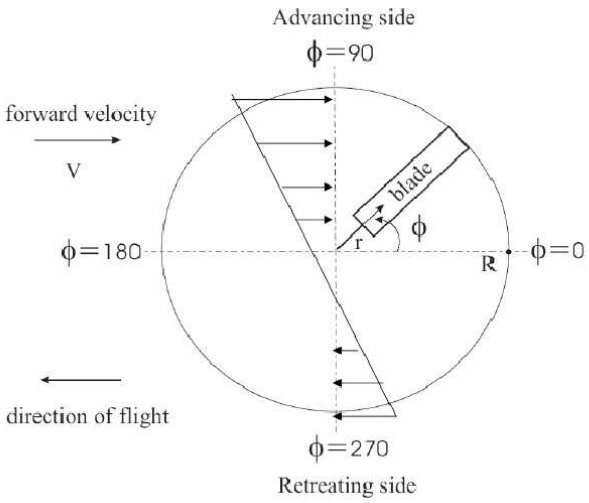

Figure 4.1: The advancing and retreating side of a blade during the forward flight.

Here μ is the advance ratio and $\Psi = \Psi_0 + \Omega t$ is the phase angle. In order to generate a uniform lift and balance the moment on the blade, the pitching angle of the blade has to be varied through

$$\theta(r, \Psi) = \theta_0 + \theta_{1c} cos(\Psi) + \theta_{1s} sin(\Psi) + ..., \tag{4.4}$$

which contains the collective pitch θ_0 and the first harmonics of the Fourier series. θ_{1c} is the lateral cyclic pitch and θ_{1s} is the longitudional cyclic pitch. On the advancing side, the effective angle is fairly low. On the retreating side the effective angle of attack is mucher higher to compensate for the reduced flow speed (Gorton & Hoad 2002). Unsteady boundary layer separation on the leading edge, initiated by the adverse pressure gradient at a high angle of attack, leads to the formation of a dynamic stall vortex. When the stall vortex resides on the blade, a significant gain in lift is observed. The stall vortex quickly detaches from the airfoil surface and is transported downsteam. Consequently, the blade experiences a drastic lost of lift and a severe increase in pitching moment. Although the flow is unsteady during forward flight, the external flow near the leading edge is quasi-steady on the local time scale. The spanwise velocity has a stronger influnce on the development of the boundary layer compared with hovering flight, but the dominant factor is the high effective angle of attack on the retreating blade causing unsteady separation. Some detailed calculations are planned.

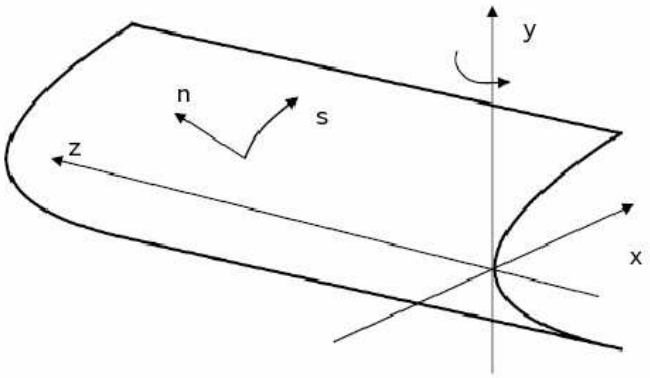

Figure 4.2: The leading edge surface of a rotating blade. $\vec{s}$ is along the tangential direction, and $\vec{n}$ is along the normal direction.

4.2 Eulerian Formulation for the Boundary Layer

In the laboratory frame, the Navier-Stoke equations for incompressible flow can be written as (see 2.9 & 2.10)

$$\frac{\partial \vec{\mathrm{v}}}{\partial \mathrm{t}} + \vec{\mathrm{v}} \times (\nabla \times \vec{\mathrm{v}}) + \frac{1}{2}\nabla(\vec{\mathrm{v}} \cdot \vec{\mathrm{v}}) = -\nabla \mathrm{p} - \frac{1}{\mathrm{Re}}\nabla \times (\nabla \times \vec{\mathrm{v}}), \tag{4.5}$$

$$\nabla \cdot \vec{\mathrm{v}} = 0. \tag{4.6}$$

As shown in Figure 4.2, the frame is attached to a blade, and rotates about the y axis with an angular speed Ω. The incident free stream is in the x-direction.

The boundary layer equations around the rotating blade are

$$\frac{\partial u^*}{\partial t^*} + u^*\frac{\partial u^*}{\partial x^*} + v^*\frac{\partial u^*}{\partial y^*} + w^*\frac{\partial u^*}{\partial z^*} = -\frac{\partial p^*}{\partial x^*} + 2\Omega w^* + \nu\frac{\partial^2 u^*}{\partial y^{*2}}, \tag{4.7}$$

$$-\frac{\partial p^*}{\partial y^*} = 0, \tag{4.8}$$

$$\frac{\partial w^*}{\partial t^*} + u^*\frac{\partial w^*}{\partial x^*} + v^*\frac{\partial w^*}{\partial y^*} + w^*\frac{\partial w^*}{\partial z^*} = -\frac{\partial p^*}{\partial z^*} - 2\Omega u^* + \nu\frac{\partial^2 w^*}{\partial y^{*2}}, \tag{4.9}$$

$$\frac{\partial u^*}{\partial x^*} + \frac{\partial v^*}{\partial y^*} + \frac{\partial w^*}{\partial z^*} = 0, \tag{4.10}$$

where $2\Omega w^*$ and $2\Omega u^*$ are due to the Coriolis force. For the boundary layer, the pressure gradients are defined by

$$
\begin{aligned}
-\frac{\partial p^*}{\partial x^*} &= \frac{\partial U_\infty}{\partial t} + U_\infty^* \frac{\partial U_\infty^*}{\partial x^*} + W_\infty^* \frac{\partial U_\infty^*}{\partial z^*} - 2\Omega W_\infty^*, \\
-\frac{\partial p^*}{\partial z^*} &= \frac{\partial W_\infty}{\partial t} + U_\infty^* \frac{\partial W_\infty^*}{\partial x^*} + W_\infty^* \frac{\partial W_\infty^*}{\partial z^*} + 2\Omega U_\infty^*.
\end{aligned} \tag{4.11}
$$

Since the flow structure near the leading edge is required, the following nondimensional variables

$$
t = \frac{t^*}{r_o/\Omega a}, \qquad Re = \frac{r_o \Omega a}{\nu}, \quad \epsilon = \frac{r_o}{a}, \tag{4.12}
$$

are introduced. Here c is the chord length, a is the radius of the blade, r_o is the nose radius at the leading edge, and Re is the local Reynolds Number. Consequently, suitable dimensionless velocity components and cooordinates are

$$
\begin{aligned}
u' &= \frac{u^*}{\Omega a}, \qquad v' = \frac{v^* Re^{1/2}}{\Omega a}, \quad w' = \frac{w^*}{\Omega a}, \\
x &= \frac{x^*}{r_o}, \qquad y = \frac{y^* Re^{1/2}}{r_o}, \quad z = \frac{z^* \epsilon}{r_o}.
\end{aligned} \tag{4.13}
$$

Similar to the two-dimenisonal boundary layer formulation, curvilinear coordinates (s, n, z) are introduced as shown in Figure 4.2. (s, n, z) are connnected with the Cartesian coordinates (x, y, z) through

$$
\mathrm{d}s = \sqrt{\xi^2 + 1}\mathrm{d}\xi, \qquad n = \eta\sqrt{\xi^2 + 1} Re^{1/2}, \tag{4.14}
$$

while

$$
x = \frac{1}{2}\left(\xi^2 - \eta^2 - 2\eta\right), y = \xi(\eta + 1) Re^{1/2}. \tag{4.15}
$$

(4.15) is the parabolic transformation used in the previous chapter. The dimensionless form of the governing equations can therefore be represented as

$$
\begin{aligned}
\frac{\partial u}{\partial t} + u\frac{\partial u}{\partial s} + v\frac{\partial u}{\partial n} + \epsilon w\frac{\partial u}{\partial z} =& \frac{\partial U_\infty}{\partial t} + U_\infty \frac{\partial U_\infty}{\partial s} + \epsilon W_\infty \frac{\partial U_\infty}{\partial z} \\
&- 2\epsilon(W_\infty - w)\frac{\xi}{\sqrt{\xi^2 + 1}} + \frac{\partial^2 u}{\partial n^2} + O(\delta),
\end{aligned} \tag{4.16}
$$

$$
\begin{aligned}
\frac{\partial w}{\partial t} + u\frac{\partial w}{\partial s} + v\frac{\partial w}{\partial n} + \epsilon w\frac{\partial w}{\partial z} =& \frac{\partial W_\infty}{\partial t} + U_\infty \frac{\partial W_\infty}{\partial s} + \epsilon W_\infty \frac{\partial W_\infty}{\partial z} \\
&+ 2\epsilon(U_\infty - u)\frac{\xi}{\sqrt{\xi^2 + 1}} + \frac{\partial^2 w}{\partial n^2} + O(\delta),
\end{aligned} \tag{4.17}
$$

$$
\frac{\partial u}{\partial s} + \frac{\partial v}{\partial n} + \epsilon\frac{\partial w}{\partial z} = 0, \tag{4.18}
$$

where $\delta = Max(\epsilon^2, 1/Re)$. As in the two-dimensional boundary layer formulation (2.18 & 2.19), the above equations are established in a coordinate system that fits the surface of the leading edge with a parabolic cylinder as shown in Figure 4.2. In the above equations, (u, v, w) are velocity components along (s, n, z), respectively.

For the current domain, s ranges over $(-\infty, \infty)$ and n ranges over $(0, \infty)$ It is convenient to map this domain to a finite one and cluster points where large gradients in the flow variables occur. The following transformation is used,

$$s = h_s(\hat{s}) = k_s \tan(\pi(\hat{s} - \frac{1}{2})), \quad n = h_n(\hat{n}) = k_n \tan(\pi\frac{\hat{n}}{2}), \quad z = \hat{z}. \tag{4.19}$$

In the new computational domain, the governing equations are

$$\frac{\partial u}{\partial t} = R\frac{\partial^2 u}{\partial \hat{n}^2} + S\frac{\partial u}{\partial \hat{s}} + T\frac{\partial u}{\partial \hat{n}} + H\frac{\partial u}{\partial \hat{z}} + K_1 + \Gamma_1, \tag{4.20}$$

$$\frac{\partial w}{\partial t} = R\frac{\partial^2 w}{\partial \hat{n}^2} + S\frac{\partial w}{\partial \hat{s}} + T\frac{\partial w}{\partial \hat{n}} + H\frac{\partial w}{\partial \hat{z}} + K_2 + \Gamma_2, \tag{4.21}$$

$$\frac{1}{h'_s}\frac{\partial u}{\partial \hat{s}} + \frac{1}{h'_n}\frac{\partial v}{\partial \hat{n}} + \epsilon\frac{\partial w}{\partial \hat{z}} = 0, \tag{4.22}$$

where the coefficients in equation (4.20)-(4.22) are

$$R = \left(h'_n(\hat{n})\right)^{-2}, \qquad S = -\frac{u}{h'_s(\hat{s})}, \tag{4.23}$$

$$T = (h'_n(\hat{n}) - v)h_n(\hat{n}), \qquad H = -\epsilon w, \tag{4.24}$$

$$K_1 = +2\epsilon w\frac{\xi}{\sqrt{\xi^2+1}}, \qquad K_2 = -2\epsilon u\frac{\xi}{\sqrt{\xi^2+1}}, \tag{4.25}$$

$$\begin{aligned}
\Gamma_1 &= \frac{\partial U_\infty}{\partial t} + U_\infty\frac{\partial U_\infty}{\partial s} + \epsilon W_\infty\frac{\partial U_\infty}{\partial z} - 2\epsilon W_\infty\frac{\xi}{\sqrt{\xi^2+1}}, \\
\Gamma_2 &= \frac{\partial W_\infty}{\partial t} + U_\infty\frac{\partial W_\infty}{\partial s} + \epsilon W_\infty\frac{\partial W_\infty}{\partial z} + 2\epsilon U_\infty\frac{\xi}{\sqrt{\xi^2+1}},
\end{aligned} \tag{4.26}$$

and $h'_s(\hat{s})$, $h'_n(\hat{n})$ are defined as

$$h'_s(\hat{s}) = \frac{dh_s(\hat{s})}{d\hat{s}} = k_s\pi\sec^2(\pi(\hat{s} - \frac{1}{2})), \quad h'_n(\hat{n}) = \frac{dh_n(\hat{n})}{d\hat{n}} = \frac{k_n\pi}{2}\sec^2(\pi\frac{\hat{n}}{2}). \tag{4.27}$$

For an impulsively started boundary layer, the initial velocity corresponds to the Rayleigh solution

$$u = U_\infty \mathrm{erf}(\hat{\rho}), \quad w = W_\infty \mathrm{erf}(\hat{\rho}), \tag{4.28}$$

where the Rayleigh variable $\hat{\rho} = \hat{n}/(2\sqrt{t})$. From lifing-line theory, U_∞ can be obtained as

$$U_\infty = z\frac{s+\alpha_e}{\sqrt{s^2+1}}. \tag{4.29}$$

W_∞ can be obtained by substituting (4.29) into (4.17) to give

$$W_\infty = \epsilon(\frac{1}{2}s^2 + (\alpha_e + \frac{\partial \alpha_e}{\partial z}z - 2)s). \tag{4.30}$$

Generally, the contribution from the trailing wake has to be included. As W_∞ is not bounded when s becomes large, the parabolic surface used in the simulation does not extend infinitely. The boundary conditions are

$$\begin{aligned} &(u,v,w) = 0 \qquad \text{at } \hat{n} = 0, \\ &u \to U_\infty(s,z), \quad w \to W_\infty(s,z) \qquad \text{as } \hat{y} \to 1. \end{aligned} \tag{4.31}$$

in which $U_\infty(s,z)$ and $W_\infty(s,z)$ are defined by the external inviscid solution. The Rayleigh solution is also implemented at upstream and downstream infinity

$$u \to U_\infty \text{erf}(\hat{\rho}), \quad w \to W_\infty \text{erf}(\hat{\rho}), \quad \text{as } \hat{s} \to \pm 1. \tag{4.32}$$

At both ends in the spanwise direction (the blade root and tip) it is assumed that

$$\frac{\partial}{\partial \hat{z}} = 0, \qquad \text{at } \hat{z} = 0, 1 \tag{4.33}$$

which reduces the boundary layer equations (4.16)-(4.18) to a quasi two-dimensional form at the root and tip. A similar approach can be found in (Atik 2002). Reduced equations at the spanwise boundaries are

$$\frac{\partial u}{\partial t} = R'\frac{\partial^2 u}{\partial \hat{n}^2} + S'\frac{\partial u}{\partial \hat{s}} + T'\frac{\partial u}{\partial \hat{n}} + {\Gamma_1}', \tag{4.34}$$

$$\frac{\partial w}{\partial t} = R'\frac{\partial^2 w}{\partial \hat{n}^2} + S'\frac{\partial w}{\partial \hat{s}} + T'\frac{\partial w}{\partial \hat{n}} + {\Gamma_2}', \tag{4.35}$$

$$\frac{1}{h_s'}\frac{\partial u}{\partial \hat{s}} + \frac{1}{h_n'}\frac{\partial v}{\partial \hat{n}} = 0, \tag{4.36}$$

where the coefficients in equations (4.34)-(4.35) are

$$R' = \left(h_n'(\hat{n})\right)^{-2}, \qquad S' = -\frac{u}{h_s'(\hat{s})}, \qquad T' = (h_n'(\hat{n}) - v)h_n(\hat{n}), \tag{4.37}$$

$${\Gamma_1}' = \frac{\partial U_\infty}{\partial t} + U_\infty\frac{\partial U_\infty}{\partial s}, \qquad {\Gamma_2}' = \frac{\partial W_\infty}{\partial t} + U_\infty\frac{\partial W_\infty}{\partial s}. \tag{4.38}$$

At the early stage of the simulation, it is convenient to introduce the Rayleigh variables

$$\rho = \frac{n}{2\sqrt{t}}, \qquad V = \frac{v}{2\sqrt{t}}. \tag{4.39}$$

Also in the computational domain, the transformed variable $\hat{\rho}$ is defined implicitly by

$$\rho = h_\rho(\hat{\rho}) = k_\rho \tan(\pi \frac{\hat{\rho}}{2}). \tag{4.40}$$

As t becomes $O(1)$, the boundary layer solution approaches the Blasius limit and the effective boundar layer shrinks to the wall in Rayleigh variables. Thus the dependent variables $(\hat{s}, \hat{\rho}, \hat{z})$ in the simulation are switched back to conventional variables $(\hat{s}, \hat{n}, \hat{z})$ at a time $t = t_d \sim O(1)$. The coeffcients k_n in (4.19) and k_ρ in (4.39) are related by

$$k_n = 2\sqrt{t_d} k_\rho. \tag{4.41}$$

The governing equations in Rayleigh variables are

$$\frac{\partial u}{\partial t} = R\frac{\partial^2 u}{\partial \hat{\rho}^2} + S\frac{\partial u}{\partial \hat{s}} + T\frac{\partial u}{\partial \hat{\rho}} + H\frac{\partial u}{\partial \hat{z}} + \Gamma 1, \tag{4.42}$$

$$\frac{\partial w}{\partial t} = R\frac{\partial^2 w}{\partial \hat{\rho}^2} + S\frac{\partial w}{\partial \hat{s}} + T\frac{\partial w}{\partial \hat{\rho}} + H\frac{\partial w}{\partial \hat{z}} + \Gamma 2, \tag{4.43}$$

and all coefficients remain the same except T, which is now

$$T = (\rho + h'_\rho(\hat{\rho}) - 2\sqrt{t}V)h_\rho(\hat{\rho})/(4t). \tag{4.44}$$

Initial and boundary conditions are implemented in (4.28)-(4.32).

4.3 Lagrangian Formulation for the Boundary Layer

As discussed at the beginning of this chapter, the Eulerian method is incapable of resolving the large gradients in the streamwise direction when the singularity begins to emerge. Therefore it is replaced by a Lagrangian method at an appropriate time, say $t = t_0$, when the boundary flow is still smooth but close to separation. The solution is continued numerically until separation occurs.

Lagrangian coordinates $(\tilde{\xi}, \tilde{\eta}, \tilde{\zeta})$ are defined as the fluid particle positions at $t = t_0$. The physical position (s, n, z) and velocity (u, v, w) of each fluid particle are functions of $(\tilde{\xi}, \tilde{\eta}, \tilde{\zeta}, t)$:

$$\begin{aligned} &s = s(\tilde{\xi}, \tilde{\eta}, \tilde{\zeta}, t), \quad n = n(\tilde{\xi}, \tilde{\eta}, \tilde{\zeta}, t), \quad z = z(\tilde{\xi}, \tilde{\eta}, \tilde{\zeta}, t), \\ &u = u(\tilde{\xi}, \tilde{\eta}, \tilde{\zeta}, t), \quad v = v(\tilde{\xi}, \tilde{\eta}, \tilde{\zeta}, t), \quad w = w(\tilde{\xi}, \tilde{\eta}, \tilde{\zeta}, t). \end{aligned} \tag{4.45}$$

The Lagrangian and Eulerian variables are related at $t = t_0$ through:

$$(s, n, z) = (\tilde{\xi}, \tilde{\eta}, \tilde{\zeta}); \quad (u, w) = (u_0(\tilde{\xi}, \tilde{\eta}, \tilde{\zeta}), w_0(\tilde{\xi}, \tilde{\eta}, \tilde{\zeta})), \qquad \text{at } t = t_0. \tag{4.46}$$

The subsequent evolution of the velocity components can be determined from the Lagrangian boundary layer equations

$$\begin{aligned}\frac{\partial u}{\partial t'} =&\frac{\partial U_\infty}{\partial t} + U_\infty \frac{\partial U_\infty}{\partial s} + \epsilon W_\infty \frac{\partial U_\infty}{\partial z} \\ &- 2\epsilon(W_\infty - w)\frac{\xi}{\sqrt{\xi^2+1}} + \frac{\partial^2 u}{\partial n^2},\end{aligned} \tag{4.47}$$

$$\begin{aligned}\frac{\partial w}{\partial t'} =&\frac{\partial W_\infty}{\partial t} + U_\infty \frac{\partial W_\infty}{\partial s} + \epsilon W_\infty \frac{\partial W_\infty}{\partial z} \\ &+ 2\epsilon(U_\infty - u)\frac{\xi}{\sqrt{\xi^2+1}} + \frac{\partial^2 w}{\partial n^2}.\end{aligned} \tag{4.48}$$

The Lagrangian derivative $\partial/\partial t'$ is

$$\frac{\partial}{\partial t'} = \frac{\partial}{\partial t} + u\frac{\partial}{\partial s} + v\frac{\partial}{\partial n} + w\frac{\partial}{\partial z}. \tag{4.49}$$

For convenience, it will be denoted as $\partial/\partial t$ in the Lagrangian analysis. Note that $\partial/\partial n$ should not appear in the governing equations; it can be replaced using the Jacobian transformation

$$\frac{\partial}{\partial n} = (x_{\tilde\zeta} z_{\tilde\eta} - x_{\tilde\eta} z_{\tilde\zeta})\frac{\partial}{\partial \tilde\xi} + (x_{\tilde\xi} z_{\tilde\zeta} - x_{\tilde\zeta} z_{\tilde\xi})\frac{\partial}{\partial \tilde\eta} + (x_{\tilde\eta} z_{\tilde\xi} - x_{\tilde\xi} z_{\tilde\eta})\frac{\partial}{\partial \tilde\zeta}, \tag{4.50}$$

so that the current particle position (s, z) can be found numerically from

$$\frac{\partial s}{\partial t} = u, \qquad \frac{\partial z}{\partial t} = \epsilon w \tag{4.51}$$

To render the Lagrangian computational domain finite, the following transformation is introduced

$$\tilde\xi = c_a \tan(\pi\hat\xi/2), \qquad \tilde\eta = c_b \tan(\pi\hat\eta/2), \tag{4.52}$$

$$s = c_a \tan(\pi\hat s/2), \qquad n = c_b \tan(\pi\hat n/2). \tag{4.53}$$

The governing equations for $\phi = u$ or w are

$$\begin{aligned}\frac{\partial \phi}{\partial t} = &P_{\hat\xi\hat\xi}\frac{\partial^2\phi}{\partial\hat\xi^2} + P_{\hat\eta\hat\eta}\frac{\partial^2\phi}{\partial\hat\eta^2} + P_{\zeta\zeta}\frac{\partial^2\phi}{\partial\zeta^2} + Q_{\hat\xi\hat\eta}\frac{\partial^2\phi}{\partial\hat\xi\partial\eta} + Q_{\hat\eta\zeta}\frac{\partial^2\phi}{\partial\hat\eta\partial\zeta} \\ &+ Q_{\hat\xi\zeta}\frac{\partial^2\phi}{\partial\hat\xi\partial\zeta} + R_{\hat\xi}\frac{\partial\phi}{\partial\hat\xi} + R_{\hat\eta}\frac{\partial\phi}{\partial\hat\eta} + R_\zeta\frac{\partial\phi}{\partial\zeta} + K_\phi + \Gamma_\phi,\end{aligned} \tag{4.54}$$

and equations (4.51) for the streamwise and spanwise particle positions are recast as

$$\frac{\partial \hat{s}}{\partial t} = \frac{2}{\pi c_a}\cos^2(\pi \hat{s}/2)\cdot u, \qquad \frac{\partial z}{\partial t} = \epsilon w. \tag{4.55}$$

The functional coefficients in equation (4.54) are defined by

$$P_{\hat{\xi}\hat{\xi}} = \tilde{\Omega}\hat{A}^2, \qquad P_{\hat{\eta}\hat{\eta}} = \tilde{\Omega}\hat{B}^2, \qquad P_{\zeta\zeta} = \tilde{\Omega}\hat{C}^2, \tag{4.56}$$

$$Q_{\hat{\xi}\hat{\eta}} = 2\tilde{\Omega}\hat{A}\hat{B}, \qquad Q_{\hat{\eta}\zeta} = 2\tilde{\Omega}\hat{B}\hat{C}, \qquad Q_{\hat{\xi}\zeta} = 2\tilde{\Omega}\hat{A}\hat{C}, \tag{4.57}$$

$$R_{\hat{\xi}} = \tilde{\Omega}\left[\left(\hat{A}\frac{\partial \hat{A}}{\partial \hat{\xi}} + \hat{B}\frac{\partial \hat{A}}{\partial \hat{\eta}} + \hat{C}\frac{\partial \hat{A}}{\partial \zeta}\right) + \hat{A}(F-H)\right], \tag{4.58}$$

$$R_{\hat{\eta}} = \tilde{\Omega}\left[\left(\hat{A}\frac{\partial \hat{B}}{\partial \hat{\xi}} + \hat{B}\frac{\partial \hat{B}}{\partial \hat{\eta}} + \hat{C}\frac{\partial \hat{B}}{\partial \zeta}\right) + \hat{B}(F-H)\right], \tag{4.59}$$

$$R_{\zeta} = \tilde{\Omega}\left[\left(\hat{A}\frac{\partial \hat{C}}{\partial \hat{\xi}} + \hat{B}\frac{\partial \hat{C}}{\partial \hat{\eta}} + \hat{C}\frac{\partial \hat{C}}{\partial \zeta}\right) + \hat{C}(F-H)\right], \tag{4.60}$$

$$\begin{aligned} K_\phi &= +2\epsilon w\frac{\xi}{\sqrt{\xi^2+1}}, \qquad \phi = u, \\ &= -2\epsilon u\frac{\xi}{\sqrt{\xi^2+1}}, \qquad \phi = w, \end{aligned} \tag{4.61}$$

$$\begin{aligned} \Gamma_\phi &= \frac{\partial U_\infty}{\partial t} + U_\infty\frac{\partial U_\infty}{\partial s} + \epsilon W_\infty\frac{\partial U_\infty}{\partial z} - 2\epsilon W_\infty\frac{\xi}{\sqrt{\xi^2+1}}, \quad \phi = u, \\ &= \frac{\partial W_\infty}{\partial t} + U_\infty\frac{\partial W_\infty}{\partial s} + \epsilon W_\infty\frac{\partial W_\infty}{\partial z} + 2\epsilon U_\infty\frac{\xi}{\sqrt{\xi^2+1}}, \quad \phi = w. \end{aligned} \tag{4.62}$$

Similarly, the coefficients in the above equations are

$$\tilde{\Omega} = \left\{\sqrt{\frac{2}{\pi c_b}}\frac{\cos(\pi\hat{\xi}/2)\cos(\pi\hat{\eta}/2)}{\cos(\pi\hat{s}/2)}\right\}^4, \tag{4.63}$$

$$\hat{A} = \frac{\partial \hat{s}}{\partial \hat{\zeta}}\frac{\partial \hat{z}}{\partial \hat{\eta}} - \frac{\partial \hat{s}}{\partial \hat{\eta}}\frac{\partial \hat{z}}{\partial \hat{\zeta}}, \quad \hat{B} = \frac{\partial \hat{s}}{\partial \hat{\xi}}\frac{\partial \hat{z}}{\partial \hat{\zeta}} - \frac{\partial \hat{s}}{\partial \hat{\zeta}}\frac{\partial \hat{z}}{\partial \hat{\xi}}, \quad \hat{C} = \frac{\partial \hat{s}}{\partial \hat{\eta}}\frac{\partial \hat{z}}{\partial \hat{\xi}} - \frac{\partial \hat{s}}{\partial \hat{\xi}}\frac{\partial \hat{z}}{\partial \hat{\eta}}, \tag{4.64}$$

$$F = \pi\tan(\pi\hat{s}/2)\left(\hat{A}\frac{\partial \hat{s}}{\partial \hat{\xi}} + \hat{B}\frac{\partial \hat{s}}{\partial \hat{\eta}} + \hat{C}\frac{\partial \hat{s}}{\partial \hat{\zeta}}\right), \tag{4.65}$$

$$H = \pi\left(\hat{A}\tan(\pi\hat{\xi}/2) + \hat{B}\tan(\pi\hat{\eta}/2)\right). \tag{4.66}$$

Initial conditions are :

$$\hat{s}(\hat{\xi},\hat{\eta},\hat{\zeta},t_0)=\hat{\xi};\quad \hat{n}(\hat{\xi},\hat{\eta},\hat{\zeta},t_0)=\hat{\eta};\quad \hat{z}(\hat{\xi},\hat{\eta},\hat{\zeta},t_0)=\hat{\zeta}. \tag{4.67}$$

$$u(\hat{\xi},\hat{\eta},\hat{\zeta},t_0)=u_0(\hat{\xi},\hat{\eta},\hat{\zeta});\quad w(\hat{\xi},\hat{\eta},\hat{\zeta},t_0)=w_0(\hat{\xi},\hat{\eta},\hat{\zeta}), \tag{4.68}$$

Boundary conditions at downstream and upstream infinity are

$$u\to U_\infty(s,z)\mathrm{erf}(\hat{\rho}),\quad w\to W_\infty(s,z)\mathrm{erf}(\hat{\rho}),\quad \text{as } \hat{\xi}\to\pm1 \tag{4.69}$$

Note that $U_\infty(x,z)$ and $W_\infty(x,z)$ have to be updated with newly computed variables x and z at each time step. Also

$$u=0,\qquad v=0,\qquad ,w=0\qquad \text{at } \hat{\eta}=0, \tag{4.70}$$

$$u=U_\infty(s,z),\quad w=W_\infty(s,z)\qquad \text{at } \hat{\eta}=1, \tag{4.71}$$

$$\hat{s}(\hat{\xi},\hat{\eta},\hat{\zeta},t)=\hat{\xi},\quad \hat{z}(\hat{\xi},\hat{\eta},\hat{\zeta},t)=\hat{\zeta}\quad \text{at } \hat{\eta}=\hat{n}=0, \tag{4.72}$$

$$\hat{s}(\hat{\xi},\hat{\eta},\hat{\zeta},t)=\pm1;\qquad \hat{z}(\hat{\xi},\hat{\eta},\hat{\zeta},t)=\hat{\zeta}\qquad \text{as } \hat{\xi}=\longrightarrow\pm1, \tag{4.73}$$

Inflow and outflow across the root and tip boundaries does have a weak effect on the interior boundary layer separation. However, this problem is expensive to handle in the Lagrangian formulation. For convenience, in some cases the spanwise velocity is assumed to be zero at the blade root and tip. Thus at the root, $w=0$ at $\hat{z}=\hat{\zeta}=0$, while at the tip, $w=0$ at $\hat{z}=\hat{\zeta}=1$. Using this, x and u can be evaluated at planes $\hat{z}=0,1$ with the assumption $\dfrac{\partial}{\partial\hat{\zeta}}=0$ (see 4.33). Following a procedure similar to that for the Eulerian calculations, the governing equations at the tip and root are

$$\frac{\partial u}{\partial t}= P'\frac{\partial^2 u}{\partial\hat{\xi}^2}+Q'\frac{\partial^2 u}{\partial\hat{\xi}\partial\hat{\eta}}+R'\frac{\partial^2 u}{\partial\hat{\eta}^2}+S'\frac{\partial u}{\partial\hat{\xi}}+T'\frac{\partial u}{\partial\hat{\eta}}+{\Gamma_u}', \tag{4.74}$$

and

$$\frac{\partial\hat{s}}{\partial t}=\frac{2}{\pi c_a}\cos^2(\pi\hat{s}/2)\cdot u, \tag{4.75}$$

for the streamwise particle positions. The functional coefficients in (4.74) are defined by

$$P'=\Omega'\left(\frac{\partial\hat{s}}{\partial\hat{\eta}}\right)^2,\qquad Q'=-2\Omega'\frac{\partial\hat{s}}{\partial\hat{\xi}}\frac{\partial\hat{s}}{\partial\hat{\eta}},\qquad R'=\Omega'\left(\frac{\partial\hat{s}}{\partial\hat{\xi}}\right)^2, \tag{4.76}$$

$$S' = \Omega' \frac{\partial \hat{s}}{\partial \hat{\eta}} \left(\frac{\partial^2 \hat{s}}{\partial \hat{\xi} \partial \hat{\eta}} - \pi \tan(\pi \hat{\xi}/2) \frac{\partial \hat{s}}{\partial \hat{\eta}} \right)$$

$$- \Omega' \frac{\partial \hat{s}}{\partial \hat{\xi}} \left(\frac{\partial^2 \hat{s}}{\partial \hat{\eta}^2} - \pi \tan(\pi \hat{\eta}/2) \frac{\partial \hat{s}}{\partial \hat{\eta}} \right), \tag{4.77}$$

$$T' = \Omega' \frac{\partial \hat{s}}{\partial \hat{\xi}} \left(\frac{\partial^2 \hat{s}}{\partial \hat{\xi} \partial \hat{\eta}} - \pi \tan(\pi \hat{\eta}/2) \frac{\partial \hat{s}}{\partial \hat{\xi}} \right)$$

$$- \Omega' \frac{\partial \hat{s}}{\partial \hat{\eta}} \left(\frac{\partial^2 \hat{s}}{\partial \hat{\xi}^2} - \pi \tan(\pi \hat{\xi}/2) \frac{\partial \hat{s}}{\partial \hat{\xi}} \right), \tag{4.78}$$

$$\Gamma_u{}' = \frac{\partial U_\infty}{\partial t} + U_\infty \frac{\partial U_\infty}{\partial s}, \tag{4.79}$$

where

$$\Omega' = \left\{ \sqrt{\frac{2}{\pi c_b}} \frac{\cos(\pi \hat{\xi}/2) \cos(\pi \hat{\eta}/2)}{\cos(\pi \hat{s}/2)} \right\}^4. \tag{4.80}$$

Boundary conditions become

$$u = 0 \quad \text{at } \hat{\eta} = 0, \qquad u = U_\infty \quad \text{at } \hat{\eta} = 1, \tag{4.81}$$

$$u = U_\infty erf(\hat{n}/(2\sqrt{t}), \qquad \hat{s} = \pm 1, \tag{4.82}$$

$$\hat{s}(\hat{\xi}, \hat{\eta}, t_0) = \hat{\xi} \tag{4.83}$$

$$u(\hat{\xi}, \hat{\eta}, t_0) = u_0(\hat{\xi}, \hat{\eta}); \qquad \hat{x}(\hat{\xi}, \hat{\eta}, t_0) = \hat{\xi}. \tag{4.84}$$

For these equations, the solution procedure can be found in Zalutsky (2000) & Atik (2002)

A singularity occurs when a stationary point emerges in the boundary layer. In another word, the coefficients of partial derivatives in (4.50) have to vanish at the same time:

$$\left(\frac{\partial \hat{s}}{\partial \hat{\zeta}} \frac{\partial \hat{z}}{\partial \hat{\eta}} - \frac{\partial \hat{s}}{\partial \hat{\eta}} \frac{\partial \hat{z}}{\partial \hat{\zeta}}, \quad \frac{\partial \hat{s}}{\partial \hat{\xi}} \frac{\partial \hat{z}}{\partial \hat{\zeta}} - \frac{\partial \hat{s}}{\partial \hat{\zeta}} \frac{\partial \hat{z}}{\partial \hat{\xi}}, \quad \frac{\partial \hat{s}}{\partial \hat{\eta}} \frac{\partial \hat{z}}{\partial \hat{\xi}} - \frac{\partial \hat{s}}{\partial \hat{\xi}} \frac{\partial z}{\partial \hat{\eta}} \right) \to 0, \tag{4.85}$$

4.4 Numerical Schemes

In the Eulerian formulation, the variables $u(s, n, z, t)$ and $w(s, n, z, t)$ are solved using a time-marching approach. For the Crank-Nicolson method, each term is averaged over the current and previous time steps so that second order accuracy in time is achieved. Central differencing is used in discretizing spatial derivatives of second

order, while first order terms are handled by upwind-downwind differencing. In this way, the coefficient matrix is diagonally dominant and the spatial resolution is also second order. Details of the numerical scheme can be found in Peridier & Walker (1989). Although the Lagrangian formulation has different variables: $u(\tilde{\xi}, \tilde{\eta}, \tilde{\zeta}, t)$, $w(\tilde{\xi}, \tilde{\eta}, \tilde{\zeta}, t)$, $s(\tilde{\xi}, \tilde{\eta}, \tilde{\zeta}, t)$, $z(\tilde{\xi}, \tilde{\eta}, \tilde{\zeta}, t)$, the same discretization ideas apply. Matrix iterations implement the ADI method, which sweeps the computational domain along grid lines. The variables on the current sweeping line are regarded as unkown while neighbouring points are assumed to be known. With boundary conditions imposed on both ends of the line, unknown variables are found using Thomas algorithm. The sweeping direction can first be chosen as the X direction so that every grid line along the X direction is succesively covered. Then the direction can be switched to Y or Z. As updated values of variables can be used directly during the sweep, the solution usually converges within 2 or 3 iterations at each time step.

Chapter 5

Three-dimensional Numerical Results

5.1 Eulerian Calculations

5.1.1 External Velocity

External velocity components in the computational domain are plotted in Figure 5.1. For an effective angle of attack, a linear twist

$$\alpha_e = 4 - 3z \tag{5.1}$$

is assumed. Downwash from the trailing wake is not included. The ratio $\epsilon = \frac{r_o}{a}$ is chosen as 0.001 and the chord thickness/length ratio is assumed to be 0.1.

In Figure 5.1(a), at a fixed section along the span, U_∞ first increases in the positive streamwise direction (from the lower surface to the upper surface). Beyond a certain maximum value, U_∞ then decreases due to the adverse pressure gradient. In Figure 5.1(b), W_∞ has a very slow variation over most of the domain in the streamwise direction. The rapid variation near $\hat{s} = 0$ or 1 is due to the transformation (4.36) used. The actual gradient of W_∞ in the streamwise direction near $\hat{s} = 0$ or 1 is small.

5.1.2 Separation Time

Boundary layer separation on the leading edge of a rotating blade is weakly three-dimensional due to the large spatial disparity between the streamwise and spanwise directions. In the streamwise direction, the velocity component has a variation $O(1)$ within a leading edge nose radius. Conversely, the spanwise velocity component has a small magnitude and a small variation over the length of the blade. In the streamwise momentum equation, to leading order, the contribution from the spanwise direction is insignificant. Strong gradients in streamwise and normal

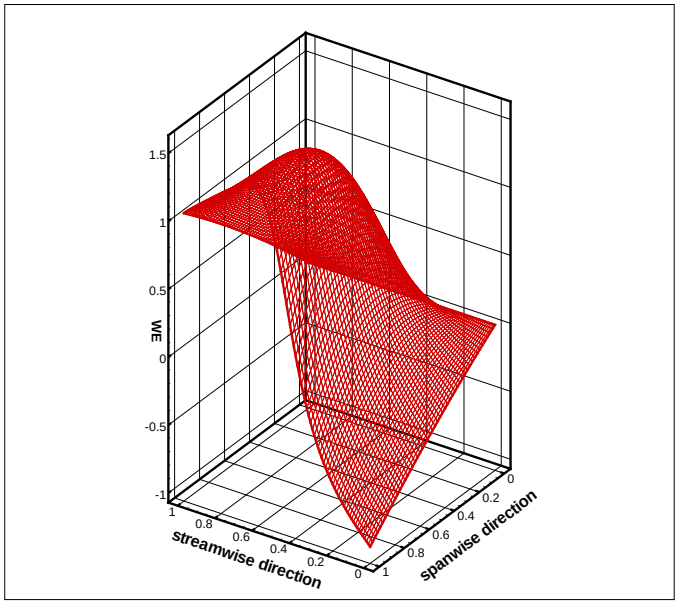

Figure 5.1: (a) The streamwise velocity in the outer flow.

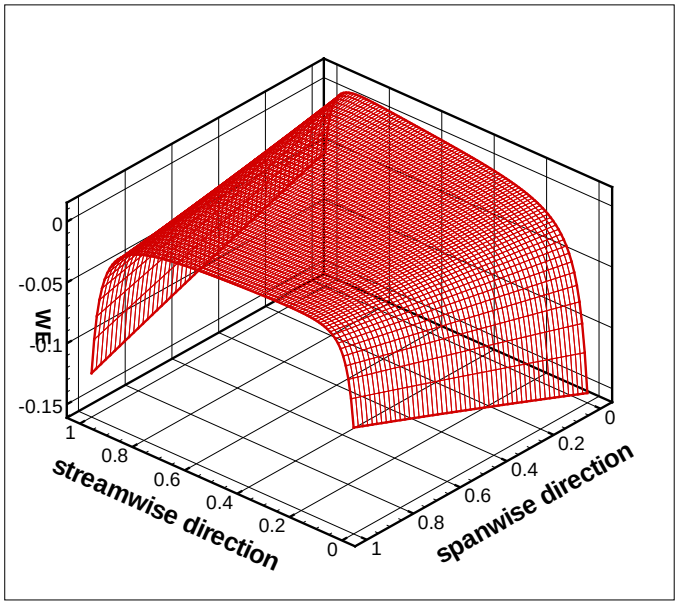

Figure 5.1: (b) The spanwise velocity in the outer flow.

velocity components are developed in a way similar to two-dimensional separation. It is expected that for certain simple conditions, such as hovering flight, separation location and time can be predicted from the two-dimensional separation results. The relation between separation time and the effective angle of attack is shown in Figure 5.2. Dimensionless variables used in the two-dimensional boundary layer studies are

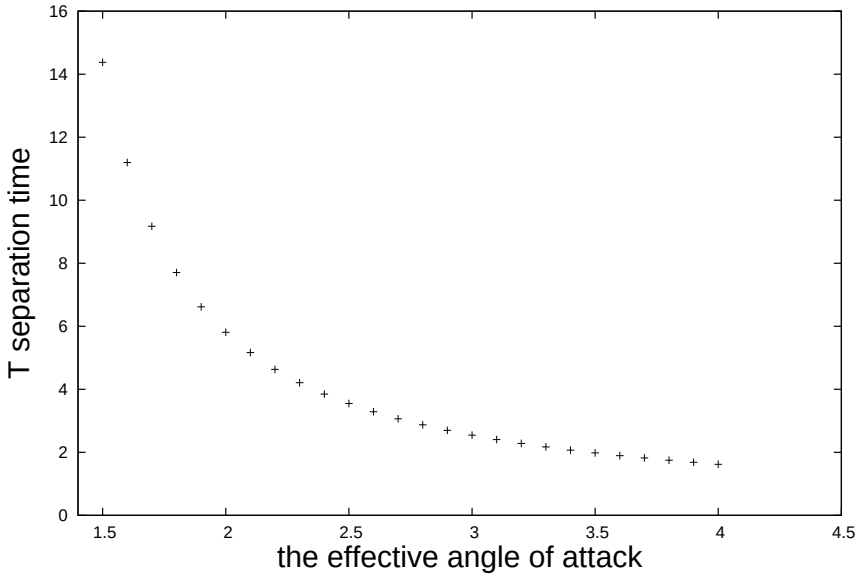

Figure 5.2: The relation between separation time and the effective angle of attack for two-dimensional leading edge separation.

$$t = \frac{t^*}{r_o/U_\infty}, \qquad u = \frac{u^*}{U_\infty}. \tag{5.2}$$

The scaled oncoming velocity is always one. For a rotating blade, the upstream flow speed varies linearly along the span. As a preliminary three-dimensional case, suppose the effective angle of attack varies along the span according to a linear twist (5.1), where downwash from the trailing wake is not included. In hovering flight, the upstream flow speed is linear

$$U_\infty = \Omega r. \tag{5.3}$$

At each cross-section, a local separation time, scaled with the local upstream velocity in (5.3), can be calculated with respect to the effective angle of attack. This trial case is displayed in Figure 5.3. The minimum separation time predicted based on the two-dimensional separation results is around 7.0 in the interval $z \in [0.4, 0.5]$ along the span. This three-dimensional separation occurs at $T = 6.69$.

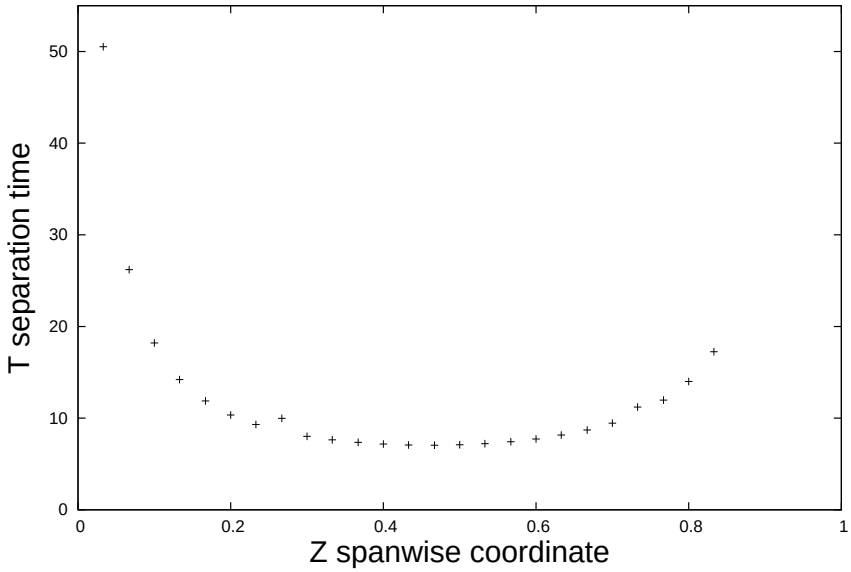

Figure 5.3: The relation between separation time and the effective angle of attack for two-dimensional leading edge separation.

5.1.3 Displacement Thickness

Three dimensional Eulerian calculations have been carried out for the boundary layer structure valid near the leading edge of a blade. The evolution of displacement thickness for the effective angle of attack (5.1) is displayed in Figures 5.4(a)-(d). In this case, the Eulerian simulation fails to converge at $t = 6.679$. As the dimensionless time t (scaled with respect to the nose radius and the blade tip speed) approaches this value, spiky behavior is seen, and indicates a local singularity. The corresponding spatial location is taken to define, approximately, the leading edge separation location. Changing the computational time step from 0.005 to 0.001 does not influence the onset and location of the singular eruption.

5.1.4 Zero Vorticity Iso-surfaces

Three-dimensional separation theory predicts that both vorticity components $\omega_z \approx -\dfrac{\partial u}{\partial y}$ and $\omega_x \approx \dfrac{\partial w}{\partial y}$ vanish when separation occurs. For a rotating blade with a high aspect ratio, however, the magnitude and direction of the spanwise velocity component only have a very weak influence on the separation location and time, but they do play a role in defining the zero iso-surface of the streamwise vorticity component. If the spanwise velocity flow is from the outboard to inboard (or $\omega_x < 0$ initially), then both zero iso-surfaces of ω_x and ω_z appear and intersect when the boundary layer nears separation, see Figure 5.5(a). Otherwise, if the spanwise

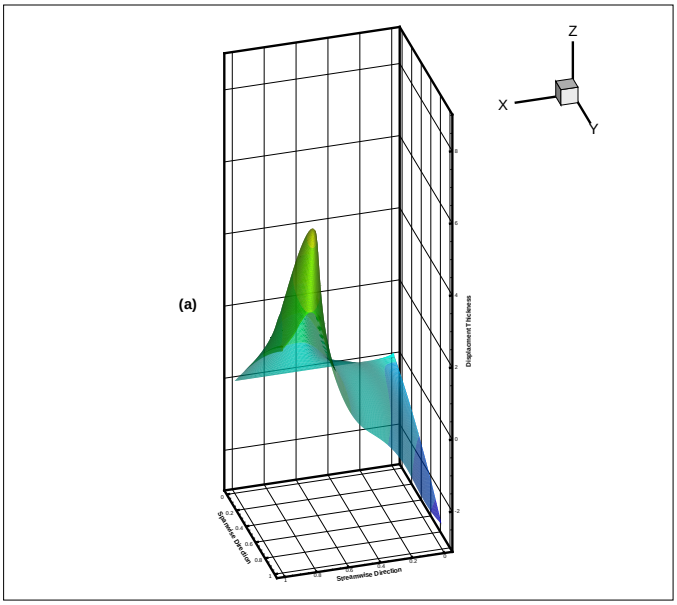
(a)
Z
X
Y
Displacement Thickness
Spanwise Direction
Streamwise Direction

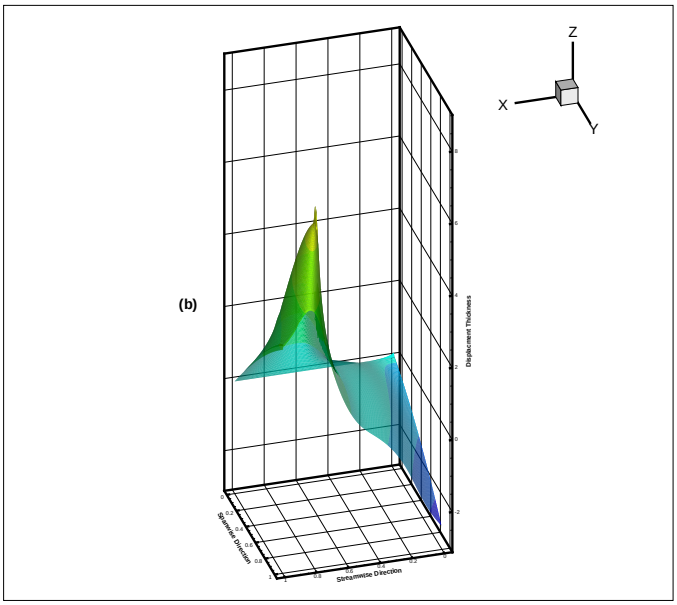
(b)
Z
X
Y
Displacement Thickness
Spanwise Direction
Streamwise Direction

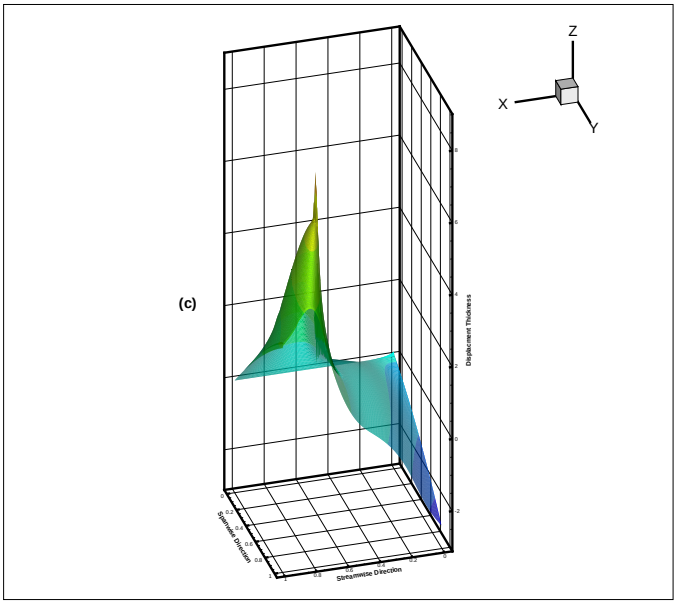

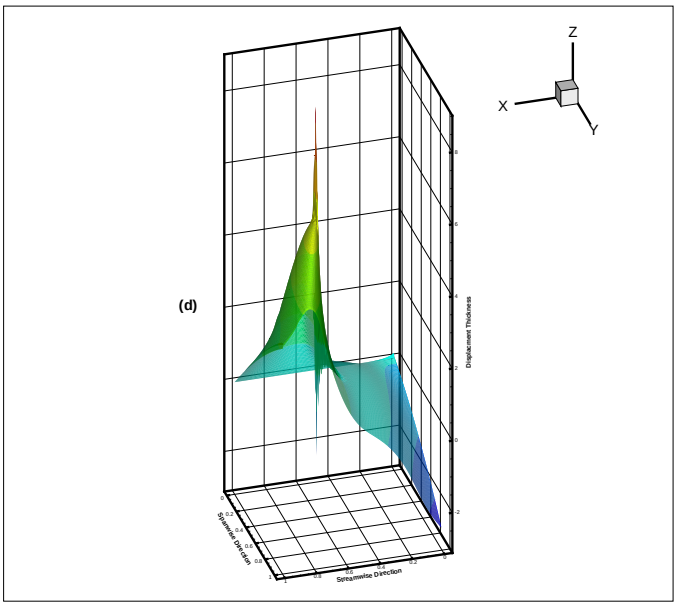

Figure 5.4: Displacement thickness at t=6.1, 6.3, 6.4, 6.5, in (a),(b),(c), (d) respectively.

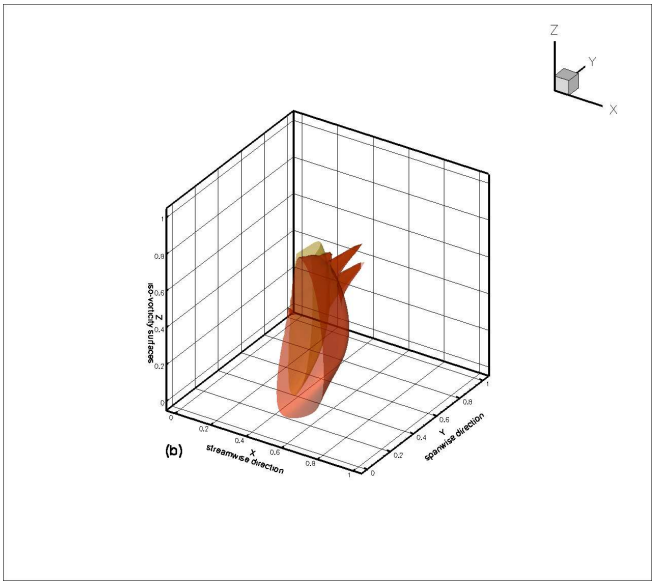

Figure 5.5: (a) Zero vorticity iso-surfaces, the red one represents ω_x and the yellow one represents ω_z.

flow is from the inboard to outboard, only the zero iso-surface of ω_z is found, and the intersection between $\omega_z = 0$ and $\omega_x = 0$ could not be determined, see Figure 5.5(b). The requirement $\omega_z = 0$ and $\omega_x = 0$ for a rigorous separation criteria comes from the idea that the displacement thickness tends to infinity, or in the continuity equation $y \to \infty$ at the singular point. For a rotating blade with a large aspect ratio the spanwise velocity has a small contribution to the continuity equation. An accurate determination of zero vorticity surface for ω_x is difficult. Nevertheless, the displacement thickness can still become very large at certain points and leads to failure of the simulation.

5.2 Separation Control

Uniform suction is implemented on the leading edge along the whole blade length. From the preliminary results, suction can considerably delay boundary layer separation on a rotating blade. In Table 5.1, suction starts from the leading edge vertex and extends over a part of the upper surface. E.g., 0.002 in Table 5.1 means 0.2 percent of chord is subject to suction.

In general, for three-dimensional flow, passive suction/injection devices can still be used, but injection should occur only where the flow will be weakly perturbed. This gives more flexibility to the control procedure.

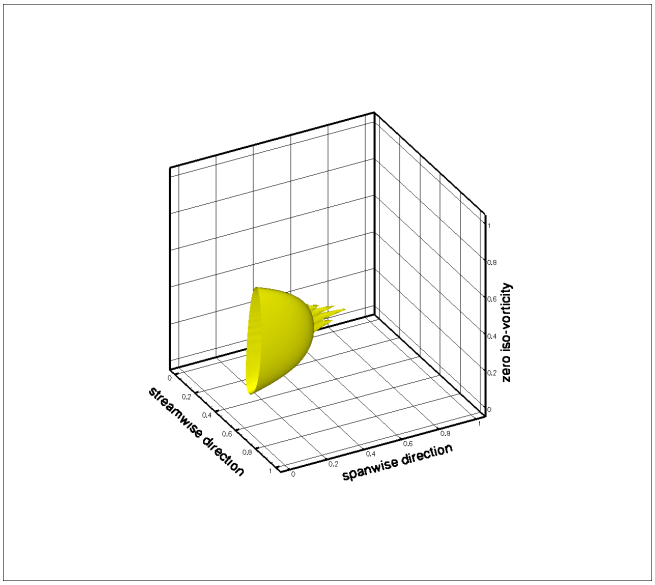

Figure 5.5: (b) Zero vorticity iso-surface, the yellow one represents ω_z.

	V_w	0.1	0.2	0.5	1.0	2.0	3.0	5.0	10.0
slots									
0.002		6.745	6.74	6.83	6.99	7.295	7.505	7.875	8.15
0.01		7	6.7	6.755	7.735	9.105	10.175	11.6	8.41
0.023		7.145	7.74	9.31	11.065	16.115	19.455	22.51	8
0.040		7.14	7.76	10.635	17.925	29.245	37.86	28.72	8.085
0.06		7.14	7.76	10.68	35.15	> 60	> 60	28.2	8.6
0.088		7.14	7.76	10.675	57.725	> 60	> 60	27.975	9.615

Table 5.1: Calculated separation time T_s with suction V_w applied on leading edge of a rotating blade

Bibliography

Atik, H., Kim, C.-Y., Van Dommelen, L. L., and Walker, J. D. A. 2002. Boundary-Layer Separation Control on a Thin Airfoil Using Local Suction. *J. Fluid Mech.* (in review).

Cowley, S. J., Van Dommelen, L. L., and Lam, S. T. 1990. On the Use of Lagrangian Variables in Descriptions of Unsteady Boundary-Layer Separation. *Phil. Trans. R. London*, **A333**, 343–378.

Degani, A. T., Li, Q., Walker, J. D. A., 1996. Unsteady Separation from the Leading Edge of a Thin Airfoil. *Physics Fluids*, **8**, 704–714.

Degani A. T., Walker J. D. A., and Smith, F. T. 1998. Unsteady Separation Past Moving Surfaces *J. Fluid Mechanics*, **375**, 1–38.

Doligalski, T. L., Smith, C. R., and Walker, J. D. A. 1994. Vortex Interactions with Walls. *Ann. Rev. Fluid Mechanics*, **26**, 573–616.

Elliot, J. W., Cowley, S. J., and Smith, F. T. 1983. Breakdown of Boundary Layers. *Geophys. Astrophys. Fluid Dyn.*, **25**, 77–138.

Gorton, S. A. and Hoad, D. R. 2002 Assessment of Rotor Blade Angle of Attack from Experimental Inflow Data. *Journal of Aircraft*, **39**, 722–730.

Karim, M. A. and Acharya, M. 1994. Suppression of Dynamic Stall Vortices Over Pitching Airfoils by Leading-Edge Suction. *AIAA J.*, **32**, 1647–1655.

Katz, J., and Plotkin, A. 2001. *Low Speed Aerodynamics*, Cambridge University Press.

Kim, C. Y. 1999. Unsteady Separation Phenomena in Two- Three-Dimensional Boundary-Layer Flows. *Ph.D. Thesis*, Lehigh University.

Leishman, J. G. 2000. *Principles of Helicopter Aerodynamics*. Cambridge University Press.

Li, H. 2000 *Formation of Rotor Tip Vortices. Master Thesis*, The Ohio State University

Milne-Thomson, L. M. 1973. *Theoretical Aerodynamics*, 4th. Edn., The Macmillan Company.

Modi, V. J., Mokhtarian, F., Fernando, M. S. U. K., and Yokomizo, T. 1991. Moving Surface Boundary-Layer Control as Applied to Two-Dimensional Airfoils. *Journal of Aircraft*, **28(2)**, 104–112.

Peridier, V. J., Smith, F. T., and Walker, J. D. A. 1991a. Vortex Induced Boundary Layer Separation. Part 1. The Unsteady Limit Problem $Re \rightarrow \infty$. *J. Fluid Mech.*, **232**, 99–131.

Peridier, V. J., Smith, F. T. and Walker, J. D. A. 1991b. Vortex-Induced Boundary Layer Separation. Part 2. Unsteady Interacting Boundary-Layer Theory. *J. Fluid Mech.*, **232**, 133–165.

Shih, C., Lourenco, L. M. and Krothapolli, A. 1995. Investigation of Flow at Leading Edge and Trailing Edges of Pitching-up Airfoil. *AIAA J.*, **33**, 1369–1376.

Srinivasan, G. R. and McCroskey, W. J. 1988. Navier-Stokes Calculations of Hovering Rotor Flowfields. *J. Aircraft*, **25**, 865–874.

Smith, C. R., Walker, J. D. A., Haidairi, A. H., and Sobrun, U. 1991. On the Dynamics of Near Wall Turbulence. *Phil. Trans. R. Soc. Lond. A*, **336**, 131–175.

Van Dommelen, L. L., and Shen, S. F. 1980. The Spontaneous Generation of the Singularity in a Separating Boundary Layer. *J. Computational Physics*, **38**, 125–140.

Van Dommelen, L. L. 1981. Unsteady Boundary-Layer Separation. *Ph.D. Thesis*, Cornell University.

Van Dommelen, L. L., and Shen, S. F. 1982. The Genesis of Separation. *In Symposium on Numerical and Physical Aspects of Aerodynamic Flows* (ed. T. Cebeci). Springer-Verlag, 293–311.

Van Dommelen, L. L. and Cowley, S. J. 1990. On The Lagrangian Description of Unsteady Boundary Layer Separation. Part 1. General Theory. *J. Fluid Mech.*, **210**, 593–626.

Van Dommelen, L. L. 1991. Lagrangian Description of Unsteady Separation. *Lectures in Appl. Math*, **28**, 701–718.

Van Dyke, M. D. 1956. Second-order subsonic airfoil theory including edge effects. *NASA TR*, **1274**.

Walker, J. D. A. 1978. The Boundary Layer Due to a Rectilinear Vortex. *Proc. R. Soc. Lond.*, A**359**, 167–188.

Wang, S. Z. 1995. Control of Dynamic Stall. *Ph.D. Thesis*, Florida State University.

Zalutsky, K. 2000. Unsteady Boundary Layer Separation. *Ph.D. Thesis*, Lehigh University.

tem Zalutsky, K., and Walker, J. D. A. 2003 Private Communication

Appendix A

Lifting-line Theory for the Downwash of a Multi-bladed Rotor with Twist in Hover

Following the approach used by Li (2000), the downwash distribution along hovering blades can be obtained from lifting-line theory. The geometric angle of attack $\alpha = \alpha(r)$, where r is the distance along the blade; $r = a$ is the blade radius. For a rectangular blade the bound circulation for a rectangular blade is given by

$$\Gamma = \pi c(\Omega \alpha r - v_z), \tag{A.1}$$

where c is the constant chord length. In (A.1), v_z is the downwash induced by the trailing vortices. The helical vortex shed between a section $(r', r' + dr')$ from a blade is assumed to be a semi-infinite cylinder, and the strength of the vortex cylinder is obtained by averaging the helical vortex over the pitch between neighbouring spirals. A semi-infinite cylinder of radius r', composed of vortex rings of constant circulation per unit length γ_θ, induces a vertical velocity

$$v_z(r) = \begin{cases} \frac{\gamma_\theta}{2}, & \text{for } r < r' \\ \frac{\gamma_\theta}{4}, & \text{for } r = r' \\ 0, & \text{for } r > r' \end{cases}, \tag{A.2}$$

For a multi-bladed rotor there are n blades. The strength of the vortex cylinder is the sum of the individual contribution from each blade. Notice in (A.2), a vortex cylinder does not induce velocity at outside points. Thus contributions to the downwash at radius r in the rotor plane are associated only with cylinders of larger radius. The net downwash is

$$v_z(r) = \frac{1}{2} \int_r^a \gamma_{\theta i}(r') dr' + \frac{1}{2} \gamma_{\theta t}, \tag{A.3}$$

where the subscripts i and t represent the inboard vortex sheet and the tip vortex respectively. In one rotor revolution, the vortex at radius r is swept downward through a distance $2\pi v_z/\Omega$. As Γ is the bound circulation along the blade, the strength of the shed circulation per unit length along the rotor is $-\dfrac{d\Gamma}{dr}$. Therefore, for a vortex cylinder with a radius r, the azimuthal component for n blades is

$$\gamma_\theta(r) = -\frac{n\Omega}{2\pi v_z(r)} \frac{d\Gamma}{dr} = -\frac{n\Omega}{2\pi v_z(r)} \left[\alpha + r \frac{d\alpha}{dr} - \frac{1}{\Omega} \frac{dv_z}{dr} \right]. \tag{A.4}$$

The vertical displacement in one revolution of the tip vortex can deduced from (A.2) as

$$\triangle z = \frac{\gamma_{\theta t}}{4}\frac{2\pi}{\Omega}, \tag{A.5}$$

where $\gamma_{\theta t}$ is the azimuthal component of vorticity at the tip. Also $\gamma_{\theta t}$ satisfies

$$\gamma_{\theta t}(r) = \frac{n\Gamma}{\triangle z} = \frac{2n\Gamma_t\Omega}{\pi\gamma_{\theta t}}, \tag{A.6}$$

which gives

$$\gamma_{\theta t}(r) = \sqrt{\frac{n\Gamma_t\Omega}{2\pi}}. \tag{A.7}$$

Substituting (A.4) and (A.7) into (A.3) leads to

$$v_z(r) = -\frac{n\Omega^2 c}{4}\int_r^a \left[\alpha + r'\frac{d\alpha}{dr'} - \frac{1}{\Omega}\frac{dv_z}{dr}\right]\frac{dr'}{v_z(r')} + \sqrt{\frac{n\Gamma_t\Omega}{2\pi}}. \tag{A.8}$$

Let α_0 be the reference angle of attack, assumed to be of the same order as the thickness/length ratio of the chord, see e.g. (2.6). After introducing the following dimensionless variables

$$\begin{aligned} R &= \frac{r}{a}, \qquad \bar{\alpha} = \frac{\alpha}{\alpha_0}, \qquad W(R) = \frac{v_z(r)}{\Omega a\alpha_0}, \\ \lambda &= \frac{\alpha_0 a}{nc}, \qquad \bar{\Gamma} = \frac{\Gamma}{\Omega ac}, \end{aligned} \tag{A.9}$$

the dimensionless downwash can be written as

$$W(R) = -\frac{1}{4\lambda}\int_R^1 \left[\bar{\alpha} + R'\frac{d\bar{(}\alpha}{dR'} - \frac{dW(R')}{dR'}\right]\frac{dR'}{W(R')} + \sqrt{\frac{1}{2\lambda}(\bar{\alpha}(1) - W(1))}. \tag{A.10}$$

At the tip,

$$W(1) = \frac{\sqrt{1 + 8\lambda\bar{\alpha}(1)} - 1}{4\lambda}. \tag{A.11}$$

Differentiating both sides of (A.10) gives

$$(1 + 4\lambda W(R))\frac{dW(R)}{dR} = \bar{\alpha} + R\frac{d\bar{\alpha}}{dR}. \tag{A.12}$$

The solution of the above equation is

$$W(R) = \frac{\sqrt{1 + 8\lambda F} - 1}{4\lambda}, \tag{A.13}$$

where

$$F = \int_R^1 \left[\bar{\alpha} + R'\frac{d\bar{\alpha}}{dR'}\right]dR' + \bar{\alpha}(1). \tag{A.14}$$

If the rotor is untwisted, or $\bar{\alpha} = \beta_0$, where β_0 is a constant, then

$$W(R) = \frac{\sqrt{1 + 8\lambda\beta_0 R} - 1}{4\lambda}. \tag{A.15}$$

If the rotor has an ideal twist, or $\bar{\alpha} = \beta_0/R$, then

$$W(R) = \frac{\sqrt{1 + 8\lambda\beta_0} - 1}{4\lambda}, \tag{A.16}$$

which is consistent with the discussion in Leishman (2000). If the rotor has a linear twist, or $\bar{\alpha} = \beta_0 - \beta_1 R$, then

$$W(R) = \frac{\sqrt{1 + 8\lambda(\beta_0 R - \beta_1 R^2)} - 1}{4\lambda}. \tag{A.17}$$

For the effective angle of attack

$$\alpha_e = \alpha - \frac{v_z}{\Omega r} \tag{A.18}$$

or

$$\alpha_e = \alpha_0 \left(\beta_0 - \beta_1 R - \frac{\sqrt{1 + 8\lambda(\beta_0 R - \beta_1 R^2)} - 1}{4\lambda R} \right) \tag{A.19}$$

in the linear case. The derivative of α_e along the spanwise direction is

$$\frac{d\alpha_e}{dR} = \alpha_0 \left(-\beta_1 + \frac{\sqrt{1 + 8\lambda(\beta_0 R - \beta_1 R^2)} - 1}{4\lambda R^2} - \frac{\beta_0 - 2\beta_1 R}{R\sqrt{1 + 8\lambda(\beta_0 R - \beta_1 R^2)}} \right) \tag{A.20}$$

At the blade root $R = 0$, α_e vanishes and its derivative along the spanwise direction is finite.